Chapter 9

General Discussion and Perspectives

> Nature's music is never over; her silences are pauses, not conclusions.
>
> Mary Webb

Thanks to a common experimental setup — the Wiper robot described in Chapter 5 —, fundamental questions in robotics and human motor control have been studied in parallel. These questions focused on the systems that are *rhythmic* (in the sense that the input command must be periodic) and *underactuated* (i.e. the actuator degrees of freedom are fewer than the system degrees of freedom). This makes the dynamics *hybrid*, since continuous-time dynamics (flight) interact with discrete-time dynamics, i.e. at impacts. Chapters 4, 6 and 7 contributed to the robotics part. They provided control design solutions for underactuated systems in which the input command influences the system state only through instantaneous impacts. Moreover, these results have been successfully validated in the lab. Chapter 8 analyzed the human behavior when controlling the *same* task, and reported different strategies depending on the context.

The aim of this general discussion is to gather the most important conclusions of the thesis, and to discuss them within the perspective of an integrated approach, between robotics and neuroscience. The discussion is divided into three sections:

- Section 9.1 is dedicated to impact juggling. We emphasize why this thesis aims at reconciling two "historically" distinct approaches for the control of impact juggling: open-loop and closed-loop. Of prime interest is the discussion of the trade-off between open-loop and closed-loop that is also present in human behaviors.

- Section 9.2 stresses the main arguments calling for an integrated approach between neuroscience and robotics. Mainly, we recall why Wiper is a unique and very appropriate setup for further investigations and experiments.

- Section 9.3 proposes a model capturing the human control strategies in bouncing experiments. The keystone of this model is to produce either discrete and individually planned movements, or rhythmic movements depending on the context.

In Section 9.4, we wrap up the central message of the thesis as a general conclusion, while in Section 9.5, we mention future perspectives and open questions in the continuity of the present manuscript.

9.1   Impact juggling control

One-dimensional impact juggling of a bouncing ball with a racket has been recognized as a benchmark in robotics and neuroscience (see Chapter 3). Despite an apparent simplicity, this task is complex, since a large number of kinematic profiles can be adopted by the racket to reach the required position and velocity at impact. From a control perspective, two approaches have been investigated for the control of this task. The *mirror law algorithms* developed by Buehler, Koditschek and Kindlmann (1988, 1990, 1994) rest on an intuitive strategy to compute the racket trajectory: the racket has to mirror the ball — up to a fixed coefficient — which is consequently permanently tracked. In 2D and 3D, further feedback loops are added to confine the ball(s) motion to vertical bouncing. The mirror law introduces sharp discontinuities in the racket trajectory at impact, due to the mirroring strategy[1]. In real-time implementations, the actual trajectory is obviously smoothed due to the n-order dynamics of the actuator. Nevertheless, the model remains valid assuming that the actuator re-tracks the "ideal" trajectory significantly before the next impact.

Sharply contrasting with the permanent tracking required by the mirror law, sensorless sinusoidal actuation achieves the stabilization of several periodic orbits in open-loop (see Holmes, 1982; Guckenheimer and Holmes, 1986; Bapat et al., 1986; Tufillaro et al., 1992; Schaal et al., 1996). Nevertheless, the parametric stability region is limited into finite ranges of both the amplitude and frequency. Schaal, Atkeson and Sternad (1996) noticed an important feature of the stabilization of the period-one (the simplest periodic orbit): the racket acceleration at impact must be *negative*, within the range defined by (3.19) according to the model. In contrast, the mirror law is closed-loop controlled and impacts the ball with positive acceleration (the mirror of the gravity).

In Chapter 7, we proposed an approach to reconcile those different strategies, i.e. to produce smooth trajectories which are based on feedback sensing. The principle of the proposed strategy is to modulate the amplitude of the sinusoidal vibration depending on the estimated velocity of the ball. The negative acceleration

---

[1]Indeed, with the mirror law, the position of the racket is continuous at impact, but the velocity obeys a discontinuous bound which is the mirror of the impact law (3.3).

at impact is then no longer required as a necessary condition for open-loop stability. However, we proved in Chapter 4 through a simplified actuation trajectory that it is a necessary condition for *robust* control. The need for robustness has been particularly emphasized in a complex impact juggling experiment, requiring the stabilization of a puck in a 2D *plane* and under "bimanual" actuation.

Such hybrid strategies (continuous actuation based on discrete feedback) have already been studied in the literature for controlling the bouncing ball, on the basis of a modulation of the sinusoidal actuation (Vincent and Mees, 2000; de Rugy et al., 2003). With respect to these earlier studies, our contributions are threefold:

1. We quantified the *robustness* of our design, and we showed that negative acceleration at impact is necessary for robust control.

2. We studied a feedback control which is only based on the detection of impact times and not on sensing the ball state, reducing the need for sensors to mere impact detectors.

3. We validated our control strategy in the lab with an actual setup that required to extend the design to a two-dimensional space.

Another contribution of the thesis was to disentangle how humans performing the same task also face the trade-off between open- and closed-loop control. We have seen that the strategy in not sensorless in normal conditions, since the suppression of visual feedback significantly altered the gain of the puck energy control loop. However, the subjects executed the task with smooth movements (either a train of discrete strokes or a sustained rhythmic actuation), sharply contrasting with the mirror law profile. Suppression of visual feedback or fast tempo favored the sustained actuation mode. This mode was sinusoidally-shaped and corresponded to negative arm acceleration at impact, highlighting the need for robust control when the sensorimotor loop was degraded.

We have not studied in this thesis to what extent the negative feedback of the energy control in the absence of visual feedback was due to (1) only the negative impact acceleration (sensorless); (2) remaining closed-loop mechanisms (due to the other sources of sensory inflow); or (3) a mixture of both of them. Based on preliminary simulation results — which are not reported in the present manuscript — we favor the third hypothesis: the sensorless sinusoidal actuation (with negative acceleration at impact) indeed results in a negative gain in the energy control loop, but much smaller than those reported in Fig. 8.5. A significant amount of this negative gain must then result from additional closed-loop mechanisms. For instance, a state observer based on impact times could be implemented on the basis of a structure similar to (7.3). Indeed, the impact times are still measurable in the absence of visual feedback both through the auditory and haptic feedback.
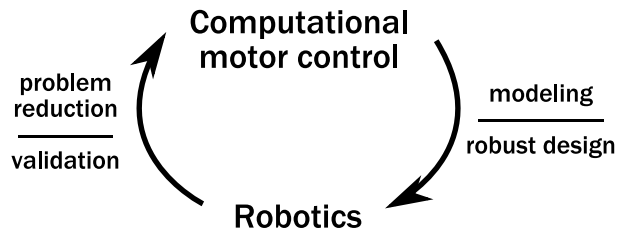
Figure 9.1: Experimental results in computational motor control and robotics cross-fertilize.

9.2   Neuroscience and robotics

The neural and behavioral study of motor control parallel with questions in robotics (mainly with humanoid robots) in many points (Schaal and Schweighofer, 2005). We tried to capture these interactions within Fig. 9.1. On the first hand, computational models can provide useful guidance in the interpretation of complex, high dimensional biological data sets. More particularly, the mathematical modeling of the task may help at reducing the problem complexity by emphasizing a limited number of relevant parameters, being useful to analyze the behavior and discriminate between different control strategies. On the other hand, models and algorithms from robotics research provide useful inspiration, baseline performance, and sometimes direct analogs for motor control.

Our study took advantage of the interaction between computational motor control and robotics. It provided a direct comparison between the theoretical predictions, the robotics implementations, and the human behavior. The data reported in Chapter 8 suggested that humans use mainly two distinct primitives to control rhythmic tasks, i.e. an intermittent train of discrete strokes or a sustained rhythmic movement. This might inspire a flexible computational model to generate complex movements, based on simple interactions between fundamental primitives.

The major contribution of the thesis in that respect was to design an original experimental setup which is easily configured for both kinds of experiments. Using the same setup and the same task, the comparison of both data sets is straightforward. For example, given the robot performance with the sensorless strategy and its lack of robustness in real experimental conditions, we anticipated that the human behavior could not be sensorless, even in the absence of visual feedback. Indeed, even in control strategies that resembled a sinusoidal actuation (sustained and sync), we have observed an active closed-loop control of the puck energy. Moreover, the negative acceleration reported with that mode was shown to be an effective measure of robustness, as illustrated in the closed-loop robotics experiment.
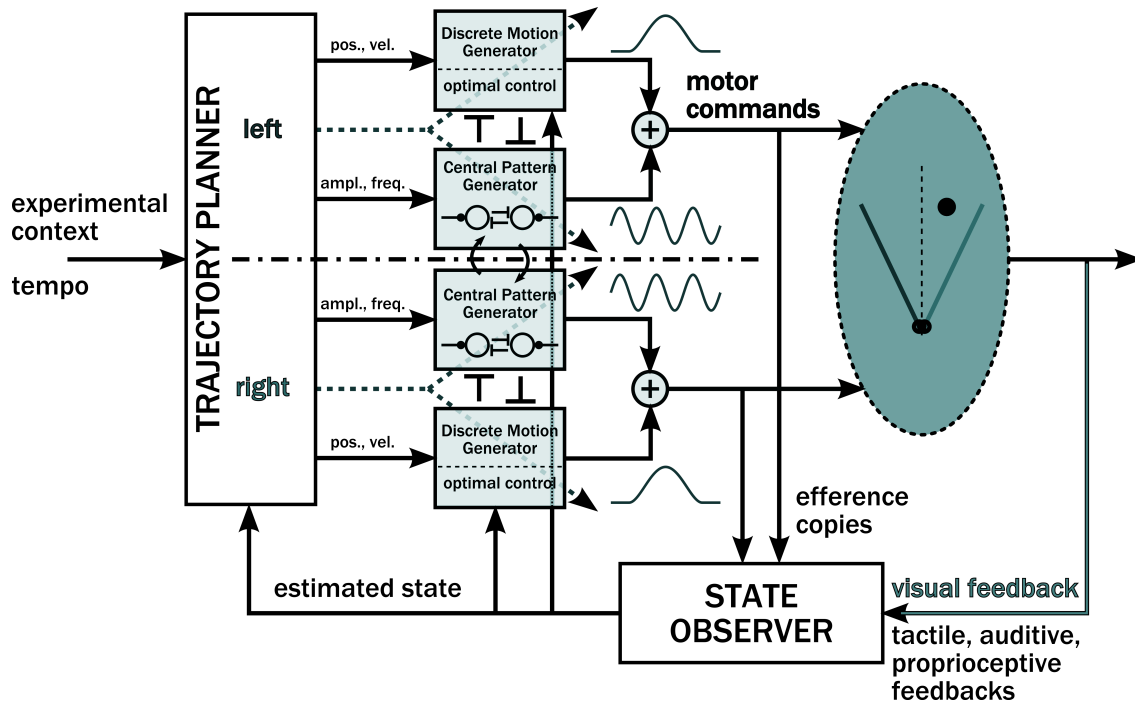
Figure 9.2: Sketch of a black-box model for the control of rhythmic tasks.

9.3   Towards a model for the control of rhythmic movements

A model capturing the observed human behavior in the control of complex impact dynamics has not been described in this manuscript, but a first sketch could be established on the basis of the conclusions of Chapter 8: the intermittent and sustained control modes are based on different fundamental primitives of movements, and consequently rest on different control architectures.

A plausible model architecture is proposed in Fig. 9.2. Its central black-box is the so-called trajectory planner (Section 1.1), which has to decide which movements will be executed depending on the experimental context (e.g. the tempo) and the available sensory feedback. The trajectory planner generates movements on the basis of two fundamental primitives:

- A discrete movement generator is used to produce individually planned discrete strokes. In this mode of control, one may hypothesize that the planning and the execution of the movement do not overlap. In impact tasks, the goal of the planned movement is to reach the desired position at the desired time, and with a desired velocity (Land and McLeod, 2000; Ronsse et al., 2007a). Optimization theory provides a computational framework which is ideal for a selection process such as motor planning (Jordan and Wolpert, 1999; Wolpert

and Ghahramani, 2000; Todorov and Jordan, 2002; Scott, 2004; Todorov, 2004, 2006).

- A central pattern generator (CPG) produces the rhythmic movement (see e.g. Cohen et al., 1988; Duysens and Van de Crommert, 1998; Swinnen, 2002; Zehr et al., 2004; White et al., 2007). In this case, we hypothesize that the trajectory planner does not plan each movement cycle separately, but rather modulates the baseline rhythmic movement (amplitude, frequency and phase). Potentially, trajectory planning and execution may overlap in this case.

The left-arm and right-arm central pattern generators are coupled with each other, in order to produce rhythmic movements which are in agreement with the well established bimanual coordination principles (Swinnen, 2002; Swinnen and Wenderoth, 2004).

The quality of the feedback path obviously depends on the available sensory inflows. In Fig. 9.2, we highlighted the visual feedback, since this particular source of information has been manipulated in the experiment reported in Chapter 8. The presence or absence of visual feedback is also the fundamental difference between the mirror law and the new family of closed-loop control strategies for bouncing tasks presented in Chapters 4 and 7. Both for our robot or for the human subjects, the quality of the state estimation (through the state observer) was significantly impaired without visual feedback, claiming for the need of a trajectory planning which is robust to these uncertainties. Consequently, the trajectory planner will favor the rhythmic central pattern generator when the state estimation is impaired due to the absence of visual feedback; or when separate planning of discrete movements is not possible given the delays in the loop. In the other cases, the trajectory planner favors the planning of intermittent discrete movements, in order to minimize the energy cost.

The model described above remains conceptual and requires further refinements.

9.4 Conclusion of the thesis

The key message of this thesis is that rhythmicity favors robustness. This has been illustrated within an integrated approach in robotics and neuroscience (motor control). In robotics experiments, we have shown that a slight modulation of a passive rhythmic actuation on the basis of limited sensing capabilities can dramatically enlarge the robustness of the control. This paradigm provides a useful guideline for the design of robots in rhythmic environments: the reduction of the sensors cost is guided by a suitable exploitation of the sensorless dynamics. The robustness of rhythmic trajectories has been confirmed by the experiments with human subjects, who sacrificed a performance index (the energy cost of their movements) to adopt a rhythmic control mode when robustness was imposed by the experimental context.

9.5 Future perspectives

At the time of completing this manuscript, a lot of exciting challenges are left unsolved. The most obvious of them is the stabilization of the n-pucks (with $n > 1$!) shower with Wiper. The most critical step toward this challenge has been solved since we succeeded to stabilize the period-two with one puck (see Section 7.3). However, two technical issues still remain before the extension to n-pucks:

The initialization: Another initialization mode has to be found, since we used the sensorless control of the period-one to initialize the movement and to let the observer converge. However, it is not possible to juggle the period-one with more than one puck.

The impact detection: The accelerometers we used would not be able to distinguish which puck impacted the arms. However, an individual processing of the feedback generated by each puck has to be computed, and the state observer of each puck could only be implemented if the setup identified which puck caused which impact.

Other research perspectives are also pointed in the continuity of the present project.

Design of continuous feedback controllers for impact tasks. The reduction of sensing capabilities is somehow pushed to the limit in the present thesis. It would be of interest to exploit the robustness analysis (which e.g. showed the importance of negative acceleration) in the design of control laws that can rely on additional sensing capabilities, e.g. a permanent tracking of the puck. It would be interesting to characterize the role of the acceleration at impact in the sensitivity to other types of perturbations, for example delays in the loop.

Vision dynamics in impact tasks. We have recorded the eye movements in the experiment reported in Chapter 8, however only static gains of vision have been analyzed in this chapter (position and velocity errors). Further analysis of the gaze dynamics would provide useful insights into the way the ocular and upper-limbs systems are coupled in juggling tasks, and to inspire humanoid robotics designs as well.

Disentangling the human control strategies. Chapter 8 focused on the human behavior to control the period-one of Wiper. However, the present analyzes capture only partially the actual control strategies. On the first hand, the differences between the discrete and the rhythmic primitives, and the subsequent trade-off between acceleration at impact and actuation energy, are reasonably clear. On the other hand, the closed-loop control of the puck energy has only been crudely understood so far. Indeed, the signature of negative feedback tuning is significant, but the low

correlation levels suggests that they only partially capture the closed-loop control. Thus these points need to be further investigated.

A model for the control of periodic movements at various tempi.   In Section 9.3, we presented a first version of a computational model aiming at reproducing the human behavior. The central question of such a model is to propose a structure which is able to produce both discrete and rhythmic movements. In the literature, this kind of model has been investigated on the basis of separate primitives (see e.g. Sternad et al., 2000) or on a similar neural architecture (see e.g. Schoner, 1990; de Rugy and Sternad, 2003; Jirsa and Kelso, 2005). However, it has never been established how the planning of either discrete or rhythmic movements could be dictated by a performance vs. robustness trade-off. Thus future perspectives include an accurate elaboration of such a model.

The role of learning.   This thesis did not focus on learning issues. Once again, this concept plays an important role, both in robotics and neuroscience: these fields may serve as a mutual source of inspiration (Schaal and Schweighofer, 2005). In behavioral experiments, learning refers to the changes in the control strategy which are only guided by the past experience and mastering in the task fulfillment. For example, it would be interesting to investigate whether the choice between the sustained or the intermittent control mode varies during the course of learning. In robotics, machine learning algorithms could also be considered to increase the controller performance on the basis of past data.

Appendices

Appendix A

Relevant Insights in Control Theory - a Benchmark Example

> There is no teaching to compare with example.
>
> ――――――――――――――――
> Sir Robert Baden-Powell

This thesis deals with several important concepts of control theory. Two of them are particularly emphasized throughout the manuscript: the balance and the complementarity between *feedback* and *feedforward* control, and the trade-off between *performance* and *robustness*. This appendix objective is to illustrate those two concepts on a simple example, in order to provide the reader with the major insights that are necessary for understanding how they are related to the rest of the thesis. The treated example belongs to the family of the *linear, time-invariant* (LTI) systems. This systems class is extremely convenient to deal with, since the mathematical tools for analysis and design are inherited from linear algebra. Nevertheless, this appendix stays also at the level of concepts, which are relevant for non-linear systems, such as the bounce jugglers presented in the other chapters.

A.1   A benchmark example

Let us consider a simple electrical DC motor as open-loop system. The motor is represented in Fig. A.1. The open-loop model can be split into an electrical and a mechanical part. The electrical part derives from the Kirchhoff's laws:

$$V_m(t) = R_m I_m(t) + L_m \frac{dI_m(t)}{dt} + k_m \omega_m(t). \tag{A.1}$$

The last term denotes the back-electromotive force, induced by the current into the rotating motor, and therefore proportional to the motor velocity. In the Laplace
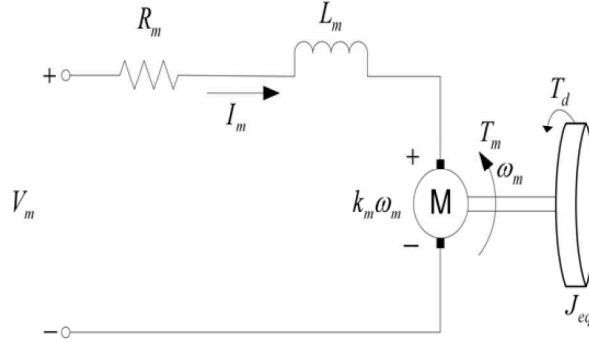
Figure A.1: Electrical DC motor.

domain, (A.1) gives:

$$V_m(s) = R_m I_m(s) + L_m s I_m(s) + k_m \Omega_m(s). \tag{A.2}$$

Assuming that the electrical time constant (L_m/R_m) is very small, and can consequently be neglected w.r.t. the mechanical time constant, (A.2) simplifies to:

$$V_m(s) = R_m I_m(s) + k_m \Omega_m(s). \tag{A.3}$$

The mechanical equation of motion of the motor derives from the rotational Newton law (the friction is neglected):

$$J_{eq} \frac{d\omega(t)}{dt} = k_m I_m(t) \tag{A.4}$$

since the motor torque is proportional to the input current. J_{eq} denotes the moment of inertia of the motor and its load. In the Laplace domain, (A.4) becomes:

$$J_{eq} s \Omega_m(s) = k_m I_m(s). \tag{A.5}$$

Combining (A.3) and (A.5), we obtain the following DC motor equation, between the voltage provided to the motor (input) and the motor velocity (output):

$$k_m V_m(s) = (R_m J_{eq} s + k_m^2) \Omega_m(s) \tag{A.6}$$

which is equivalent to the following open-loop transfer function:

$$G_m(s) \equiv \frac{\Omega_m(s)}{V_m(s)} = \frac{k_m}{R_m J_{eq} s + k_m^2} = \frac{K}{\tau s + 1} \tag{A.7}$$

where the open-loop gain and the open-loop time constant are equal to $K = 1/k_m$ and $\tau = R_m J_{eq}/k_m^2$. The (realistic) numerical values used in the rest of this section are $K = 20\text{rad/Vs}$ and $\tau = 0.1\text{s}$.

A.2   Feedback and feedforward control

The term *feedback* is used to refer to a situation in which two (or more) dynamical systems are connected together such that each system influences the other and their dynamics are thus strongly coupled (Astrom and Murray, 2005). In the treated example, one system is the motor, and the second is a *controller*. The coupling from the controller to the motor is obvious, since the controller assigns the input voltage of the motor. The motor state influences also the controller, since its output (i.e. the motor velocity) is *measured* to adapt the controller output (i.e. the motor voltage) consequently. The classical feedback loop is depicted in Fig. 1.2(b): the controller C_{FB} updates the system input $u(t)$ (the voltage in this case), depending on the difference between the reference signal $r(t)$ and the actual measured output $y(t)$ (the motor velocity in this case).

Usually, we may summarize the advantage of feedback control in three points:

- Feedback can be used to stabilize unstable open-loop dynamics. Nevertheless, this is not the case of the DC motor (A.7).

- Feedback can be used to speed up the dynamics, by tuning the closed-loop bandwidth at a larger value than the open-loop one.

- Feedback enhances the system *robustness* with respect to uncertainties or perturbations.

For example, imagine that the requirements of the loop design are: asymptotic tracking (zero static error), no overshoot, and doubling of the open-loop bandwidth in closed-loop, i.e. $\omega_0 = 1/0.05 = 20$rad/s. A first naive approach to design a controller respecting these requirements is to do *feedforward* control, according to an architecture relaxing the need of sensors (see Fig. 1.2(a)). Indeed, in such a structure, the output $y(t)$ has not to be measured to compute the input signal $u(t)$. Moreover, given the open-loop transfer function (A.7), a feedforward controller which respects all of the design requirements can be straightforwardly derived:

$$C_{FF}(s) = \frac{0.1s + 1}{20(0.05s + 1)} \tag{A.8}$$

and the step response of the corresponding transfer function $C_{FF}(s)G_m(s)$ is given in Fig. A.2(a), black line. The step response has indeed no static error (the static gain equals 1); the settling time[1] is about 0.19s, i.e. twice faster than the open-loop; and there is no overshoot, since the resulting dynamics is of first order.

However, when studying the controller performance with respect to unexpected *perturbations*, Fig. A.2(a) reveals large discrepancies between the desired and the actual behavior. Indeed if the gain K varies of $\pm 20\%$ (red curves), the static error is now of the same order of variation. If the time constant τ varies of $\pm 20\%$ green

---

[1]I.e. the time from which the step response enters forever into a "tube" of 5% of its final value.

curves), the settling time is much larger in one case, while there is overshoot in the other. In real systems, it is tedious to identify the open-loop parameters with more than 20% of accuracy. Moreover, there is usually unexpected (or unmodeled) perturbations in the dynamics that cause variability of (at least) the same order of magnitude. Feedback is consequently mandatory to make a system robust to such perturbations.

The classical closed-loop approach to achieve asymptotic tracking, despite perturbations, is to do *proportional-integral* (PI) control:

$$
\begin{aligned}
u(t) &= k_p \left(b_{sp}r(t) - y(t)\right) + k_i \int_0^t \left(r(\tau) - y(\tau)\right) d\tau \\
&= k_p \left(r(t) - y(t)\right) + k_i \int_0^t \left(r(\tau) - y(\tau)\right) d\tau + k_p(b_{sp} - 1)r(t). \quad \text{(A.9)}
\end{aligned}
$$

The first term of (A.9) is proportional to the difference between the reference and the actual output. The second term of (A.9) is proportional to the *integral* of the difference between the reference and the actual output. The third term of (A.9) is directly proportional to the reference and is therefore a (static) feedforward part. The "magic" of the integral action is that it always cancels the static error, if the closed-loop system is stable. Indeed, when $u(t)$ has reached its steady-state, the integrand of (A.9) has to be zero, and thus $y(t) = r(t)$, as $t \to +\infty$.

Assuming first that $b_{sp} = 1$ (no feedforward control), such that the closed-loop design corresponds to Fig. 1.2(a), the transfer function of the controller is given by:

$$
C_{FB}(s) = k_p + \frac{k_i}{s} = \frac{k_p s + k_i}{s} \quad \text{(A.10)}
$$

and the corresponding closed-loop transfer function equals:

$$
\frac{C_{FB}(s)G_m(s)}{1 + C_{FB}(s)G_m(s)e^{-\Delta s}} = \frac{K(k_p s + k_i)}{\tau s^2 + (1 + Kk_p e^{-\Delta s})s + Kk_i e^{-\Delta s}}. \quad \text{(A.11)}
$$

Neglecting the delay ($\Delta \simeq 0$), the gains k_p and k_i are used to *place the poles* of the closed-loop transfer function at the desired location. One may choose them to equal the denominator of (A.11) with the following characteristic polynomial: $s^2 + 2\zeta\omega_0 s + \omega_0^2$, where ζ is the desired damping factor and ω_0 is the desired natural frequency. This gives:

$$
k_p = \frac{2\zeta\omega_0\tau - 1}{K}, \quad \text{(A.12)}
$$

$$
k_i = \frac{\omega_0^2\tau}{K}. \quad \text{(A.13)}
$$

The design objectives invite to choose $\zeta = 1$ (critical damping factor, i.e. no overshoot) and obviously $\omega_0 = 20\text{rad/s}$. The corresponding gains are $k_p = 0.15$ and $k_i = 2$.

The step response of the so-designed closed-loop DC motor is given in Fig. A.2(b) (with $\Delta = 0.01$s). As expected, PI control ensures a zero static error whatever the perturbations. In general, the five curves are close to each other.

The 5% overshoot of the closed-loop step response (black curve in Fig. A.2(b)) is due both to the delay — not accounted for in the design — and to the *zero* (i.e. the first order term of the numerator) of the closed-loop transfer function (A.11). This turns the dynamics to be more reactive than the "pure" second order we have designed. Nevertheless, this zero can also be freely placed by considering *feedforward* control ($b_{sp} \neq 1$), above the feedback loop (Fig. 1.2(c)). By considering simply a static feedforward gain, i.e. $C_{FF}(s) = k_p(b_{sp}-1)$, the loop transfer function becomes:

$$\frac{\frac{b_{sp}k_ps+k_i}{s}G_m(s)}{1 + \frac{k_ps+k_i}{s}G_m(s)e^{-\Delta s}} = \frac{K(b_{sp}k_ps + k_i)}{\tau s^2 + (1 + Kk_pe^{-\Delta s})s + Kk_ie^{-\Delta s}} \qquad (A.14)$$

and the zero of (A.14) can be placed with b_{sp}, i.e. the feedforward gain.

As an example, we may place the zero to cancel one of the closed-loop poles, i.e. $k_i/(b_{sp}k_p) = \omega_0$. This gives $b_{sp} = \omega_0\tau/(2\zeta\omega_0\tau - 1) = 0.67$, assuming that the other gains remain unchanged. The corresponding step responses to the nominal and perturbed motor transfer functions are given in Fig. A.2(c). There is no overshoot anymore in the step response of the nominal transfer function, since it reduced to first order (neglecting the delay). Asymptotic tracking is still achieved whatever the perturbation, and the settling time corresponds to the requested one. Note that more complex designs could be made by adding dynamical terms to the feedforward path.

In summary, the feedback is highly efficient to make the design robust to unexpected variations in the open-loop transfer function, or to external perturbations. The feedforward is complementary to the feedback, since it adds new degrees of freedom to the design. Moreover, since the feedforward part does not rest on sensory measurements, it may considerably facilitate the system design if robust enough: some state variables are indeed very hard to measure, while sensory processing is inherently subject to delays. . .

A.3   Robustness vs. performance

The previous section has already emphasized the role of feedback to strongly increase the robustness of a given system. This section objective is to rapidly overview some concepts which *quantify* the robustness of any LTI closed-loop system. Moreover, we shall see that increasing the robustness of the previous design can only be made by degrading its *performance*.

Two important transfer functions to study the robustness of a closed-loop system are called the *sensitivity function $S(s)$* and the *complementary sensitivity function*

$T(s)$:

$$S(s) = \frac{1}{1 + C_{FB}(s)G(s)}, \tag{A.15}$$

$$T(s) = \frac{C_{FB}(s)G(s)}{1 + C_{FB}(s)G(s)}. \tag{A.16}$$

They capture respectively the closed-loop sensitivity w.r.t. to small variations in the process ($S(s)$), and large variations in the process ($T(s)$). They are said to be complementary since $S(s) + T(s) = 1$. In general, it is important to minimize these functions, in order to keep the closed-loop system robust to both the unexpected perturbations (typically at low frequencies) and the noise (typically at high frequencies). In order to minimize these functions, the problem can be reduced to minimize their maximum M_S and M_T.

Fig. A.2(d) displays the maximum of the sensitivity functions, namely M_S and M_T[2], for different closed-loop designs corresponding to different natural frequencies ω_0, while considering $b_{sp} = 1$ (no feedforward control, for simplicity). The delay is still equal to $\Delta = 0.01$s. As depicted in this figure, the initial design, i.e. $\omega_0 = 20$rad/s, is not optimal to minimize the maximum of the sensitivity functions. Conversely, we may choose $\omega_0 \simeq 7$rad/s to minimize M_S, while keeping M_T reasonably bounded. Note however that this closed-loop natural frequency is even smaller than the open-loop one, since the delay has been detrimental for the sensitivity functions.

The second design is then more robust than the first one. This is further confirmed by Fig. A.2(e) which displays the Nyquist plots of both loop functions. The stability margins, i.e. the gain and phase distances between the curve and the point of instability $(-1, 0)$, are larger for the second design (blue).

Nevertheless, the increase in robustness has been obtained by reducing the natural frequency (i.e. the closed-loop bandwidth), resulting in a decrease in performance. Indeed, the settling time corresponding to the second design (small bandwidth) is much larger than the settling time corresponding to the first design (see Fig. A.2(f)).

In general, performance and robustness of closed-loop systems cannot be arbitrarily increased simultaneously and result from a design trade-off.
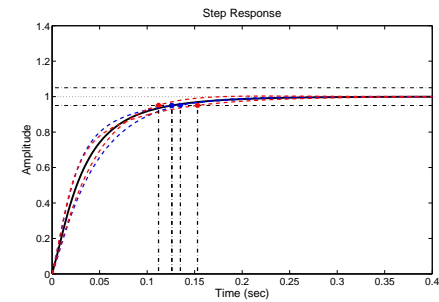
---

[2]For computational simplicity, we have appended the sensory delay directly to the open-loop transfer function: $G_m(s) = Ke^{-\Delta s}/(\tau s + 1)$.
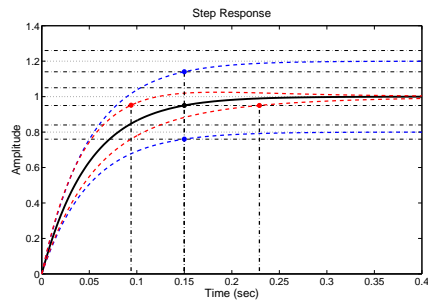
(a) Forward controller.
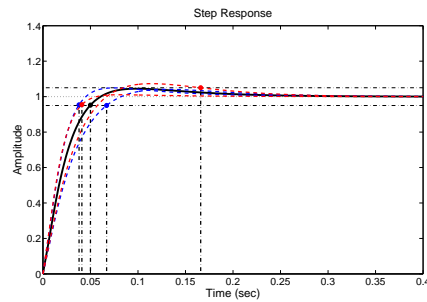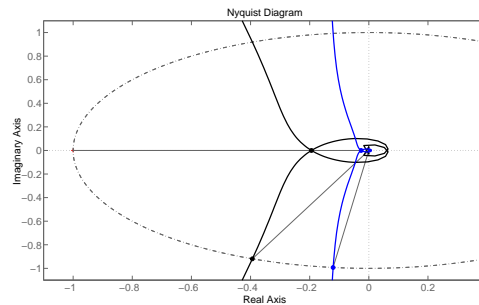
(b) Closed-loop controller.

(c) Combined feedback+feedforward controller.

(a), (b) and (c) Step responses to the nominal transfer function (A.7) (black), the transfer function with an error of $\pm 20\%$ in the gain K (blue), and the transfer function with an error of $\pm 20\%$ in the time constant τ (red). The corresponding settling times are represented by colored dots, and vertical lines.
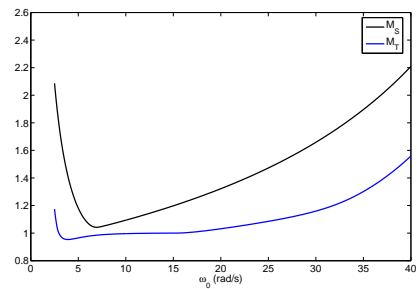
(d) Maximum of the sensitivity function $S(s)$ (M_S, black) and the complementary sensitivity function $T(s)$ (M_T, blue) for different closed-loop natural frequencies ω_0.

(e) Nyquist plots and stability margins of $C_{FB}(s)G_{m2}(s)$ where the design is made for $\omega_0 = 20\text{rad/s}$ (black) and $\omega_0 = 7\text{rad/s}$ (blue).
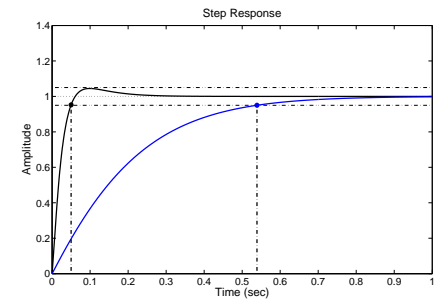
(f) Step responses of the closed-loop controller to the nominal transfer function (A.7) with the designed closed-loop bandwidth at $\omega_0 = 20\text{rad/s}$ (black) and $\omega_0 = 7\text{rad/s}$ (blue). The corresponding settling times are represented by colored dots, and vertical lines.

Figure A.2: Figures related to Appendix A.

Appendix B

Major Technical Characteristics of the Experimental Setup

> Technical skill is mastery of complexity, while creativity is mastery of simplicity.
>
> ——————————————————
> Erik Christopher Zeeman

This appendix provides the main technical details about the practical implementations of the Wiper robot, presented in Chapter 5. Section B.1 describes the technical configuration of the setup in the "robotics" version. This configuration was used for experimental validations, reported in Chapters 6 and 7. Section B.2 refers to the "human" configuration, used for a motor control investigation on human juggling, reported in Chapter 8.

B.1 Technical details about the robotics configuration of Wiper

In the present section, we will give the main details about the technical implementation of Wiper which led to robotics experiments. These experiments are reported in Chapters 6 (sensorless control) and 7 (feedback control). A general picture of the setup in this configuration is provided in Fig. 5.3.

B.1.1 Hardware description

Air hockey table

The air-hockey table dimensions are given in Fig. B.1. A supporting structure has been manufactured such that the table can be tilted between 0° and 45° thanks to an electrical power jack (Servomech, see Fig. B.2). The air-hockey table is pierced with
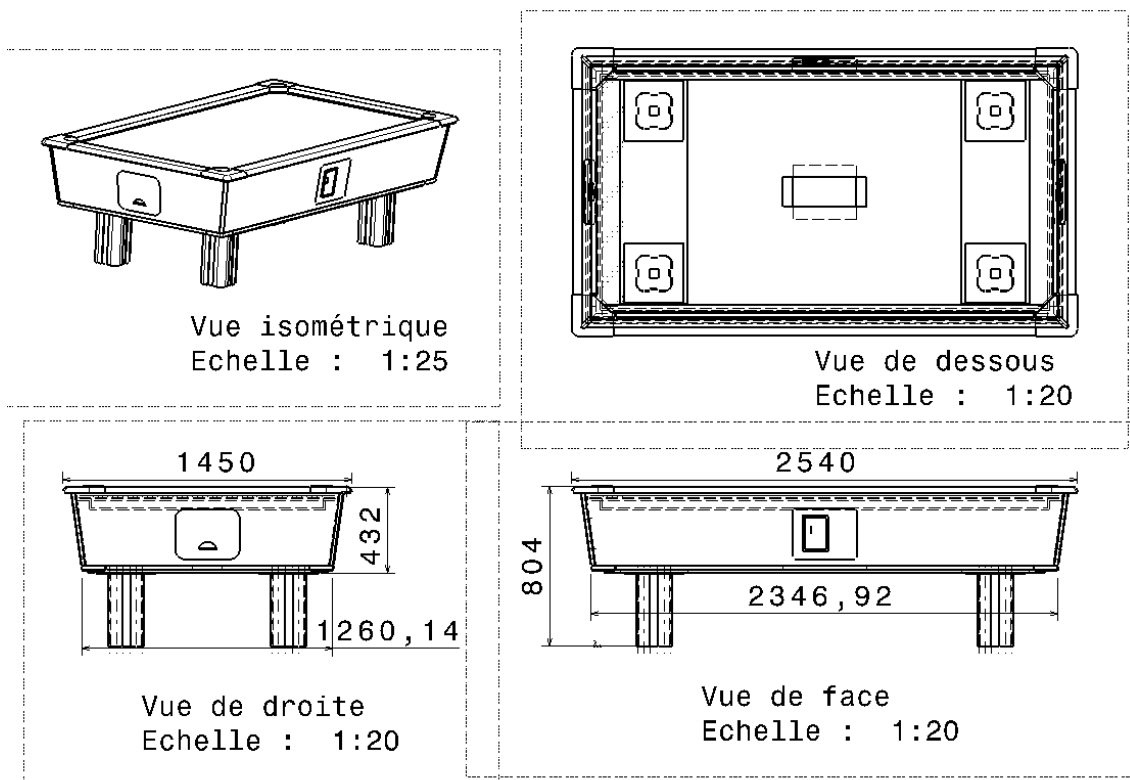
Figure B.1: Dimensions of the air-hockey table [mm].

Figure B.2: Electrical power jacks.

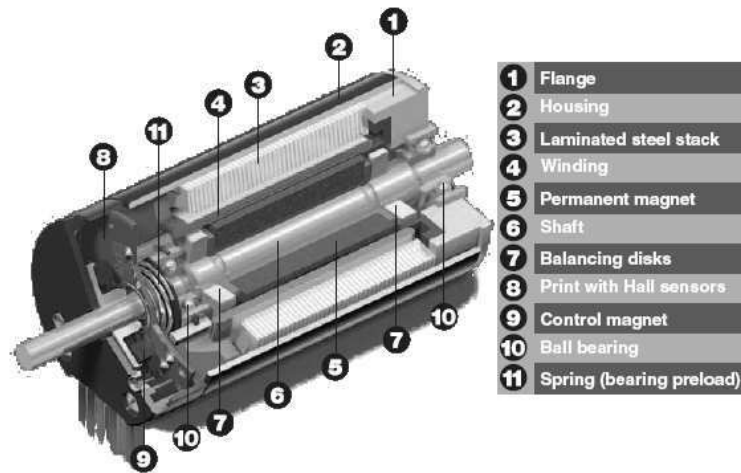| 1 | Flange |
2	Housing
3	Laminated steel stack
4	Winding
5	Permanent magnet
6	Shaft
7	Balancing disks
8	Print with Hall sensors
9	Control magnet
10	Ball bearing
11	Spring (bearing preload)

Figure B.3: Scheme of a brushless EC motor (Maxon Motor company).

a lattice of little holes, separated about 4cm from each other. Constant air blowing
through the holes provides frictionless motion of the sliding bodies. The robotics
experiments have been conducted with 12.5° of table inclination. This provided
comfortable cycles frequencies for experimental supervision. Note moreover that
the gravity constant **g** plays no role in the analysis further derived.

Motors and edges

The 1m-long impacting edges were manufactured in aluminium, to be both light
and rigid. They are actuated around their lower extremity by two independent DC
motors. The motors are mounted on the rigid frame of the table, close to each other
(about 10cm) since the model assumes that both edges rotate around the same point.
Given the typical velocity and acceleration of the edges trajectory, we estimated
the maximum rotational velocity of the motor at 4500RPM, producing a maximal
torque of 55mNm (the corresponding power is then 25W). These requirements are
met with by the EC40-118896 motor (electronically commuted, see Fig. B.3) +
GP42C-203129 planetary gearhead manufactured by the Maxon Motor company
(`www.maxonmotor.com`, Sachseln, Switzerland).

The motor is also equipped with a digital-encoder (incremental), in order to
reconstruct its rotational velocity. The encoders are HEDL 5540 (Maxon Motor
company).

The primary motor control loop is velocity control. It is insured through two
independent servoamplifiers, one for each motor (model DES50/5, 4 quadrants op-
erational, Maxon Motor company, see Fig. B.4). The PI velocity controllers are
factory-designed to provide excellent dynamical performances with no static error.
The servoamplifier received the digital-encoder signals as inputs and provided the
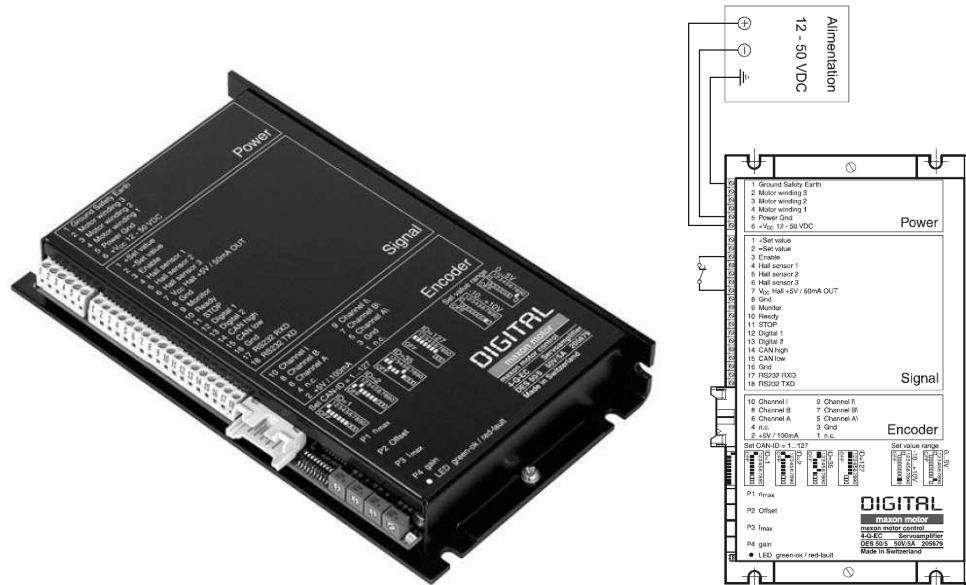
Figure B.4: DES50/5 servoamplifier (Maxon Motor company).

motor voltage as output. The external input, provided to the servoamplifier, is obviously the desired motor velocity.

Position sensor units

In order to realize *position* control of the juggling edges, we superimposed a second loop above each servoamplifier. The position sensors have been custom-made. Their input is the digital-encoder signals, while they outputted the current motor position. The block diagram of the position control loop is given in Fig. B.5. The reference position is derived and directly provided as voltage set value (referenced velocity), through a feedforward (FF) gain (upward path). The feedback part compares the reference with the real measured position and updates the controller output (voltage set value) accordingly, through proportional (P) and derivative (D) gains. No integral gain is necessary to insure zero static error in the output/reference transfer function, since the "plan" is an integrator: the measured output is the position while the plan input is the desired velocity.

Accelerometers

In order to validate closed-loop mechanism described in Chapter 4 with Wiper, we had to detect the impact times. This has been realized with two accelerometers mounted at the top of the edges to record the high-frequency small vibrations generated by the impacts. The accelerometers raw signals were high-pass filtered to remove the accelerations induced by regular edge motion (low frequencies). The
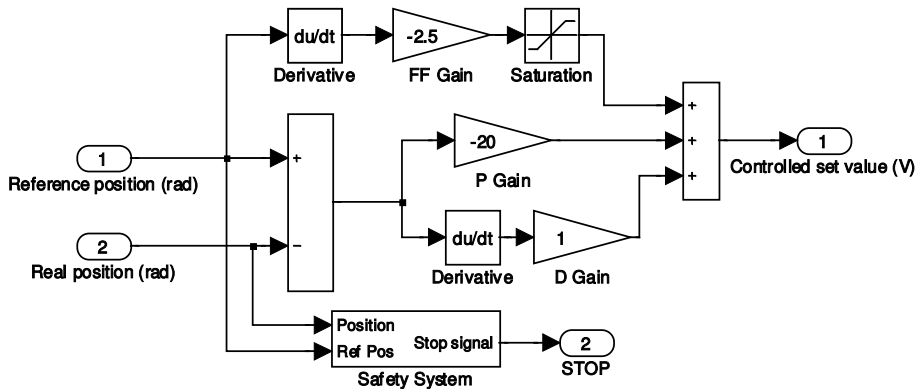
Figure B.5: Block diagram (Simulink) of the position unit.

design has been made on a Chebyshev digital filter (type II) with MATLAB (The
Mathworks Inc., Natick, MA). This filter was designed to lose no more than 1dB in
the passband [150Hz,. . .] and to have at least 80dB of attenuation in the stopband
[0Hz,1Hz]. The attenuation was smooth between 1Hz and 150Hz, such that the filter
order was limited (second order). Consequently, its transfer function was:

$$0.83\frac{z^2 - 2z + 1}{z^2 - 1.63z + 0.69}.$$

Computer control

The processing of the accelerometers high-pass filter, the motors position controllers,
and, more importantly, the planning of the actuation profiles, were implemented in a
dedicated computer. These programs were written with XPCTARGET, a Simulink-
oriented software (The Mathworks Inc., Natick, MA). This software self-generated
the executable code, and uploaded and executed it in another dedicated (target)
computer, running the real-time operating system.

B.1.2   Programs architecture

Sensorless control

Open-loop sinusoidal actuation of the arms conducted to sensorless stabilization
of periodic orbits in Wiper (see Chapter 6). The Simulink diagram corresponding
to this "controller" is represented in Fig. B.6. The sinusoidal signal, at the desired
amplitude and frequency, is directly provided as reference to two position controllers
(pictured in Fig. B.5): one for each arm. The measured position signals are also
provided. Note moreover that several security and protection boxes have been added
to provide major damages to the setup, due for example to large differences between
the referenced and the actual position. The algorithm sampling frequency was 1kHz
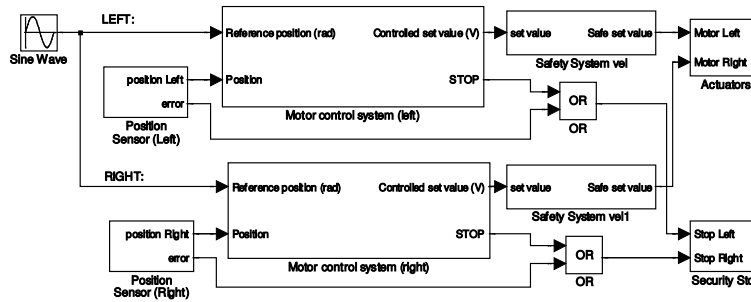(1ms as sampling interval).

Figure B.6: Block diagram (Simulink) of the sensorless controller.

Feedback control

The closed-loop controller, based on impact times detection, is pictured in Fig. B.7.
The figure is divided in 5 colored parts. The gray part is the actual setup, whose
inputs are the voltage set values of the motors servoamplifiers, and outputs (in red)
are the measured positions of the motors, and accelerometers raw signals. The
white part is the position control unit of both edges, already described previously
(the security blocks have been removed for clarity). The red part is the signal
processing unit of the accelerometers data. It outputs two triggering signals (one
for each arm) that rise when an impact is detected. The blue part is the observer
(see (7.3)), which provides an estimate of the puck state at impact, on the basis of
the motors position signals, and the detected impact times. Finally the green part
is the planner, which constructs the reference signals of the tracking controller (7.8),
on the basis of the estimated state variables. The algorithm sampling frequency was
333Hz (3ms as sampling interval).

B.2   Technical details about the "human" configuration of Wiper

In the present section, we will give the main details about the technical implemen-
tation of Wiper which led to human motor control experiments. These experiments
are reported in Chapter 8. A general picture of the setup in that configuration is
provided in Fig. 5.2.

The air-hockey table was the same as described in Section B.1.1, also tilted
at 12.5° w.r.t. the ground. We replaced the actuated edges by two steel-plain
arms. These arms rotated freely around their lower extremity, being axial rotating
joins, and the subjects controlled the arms angular position through direct catching.
For prehension facility, a thin metallic profile was fixated on the arms top surface.
The position of the arms and the puck were recorded by an Optotrak for off-line
processing, as reported in Section 8.1. A digital metronome was used to beep the

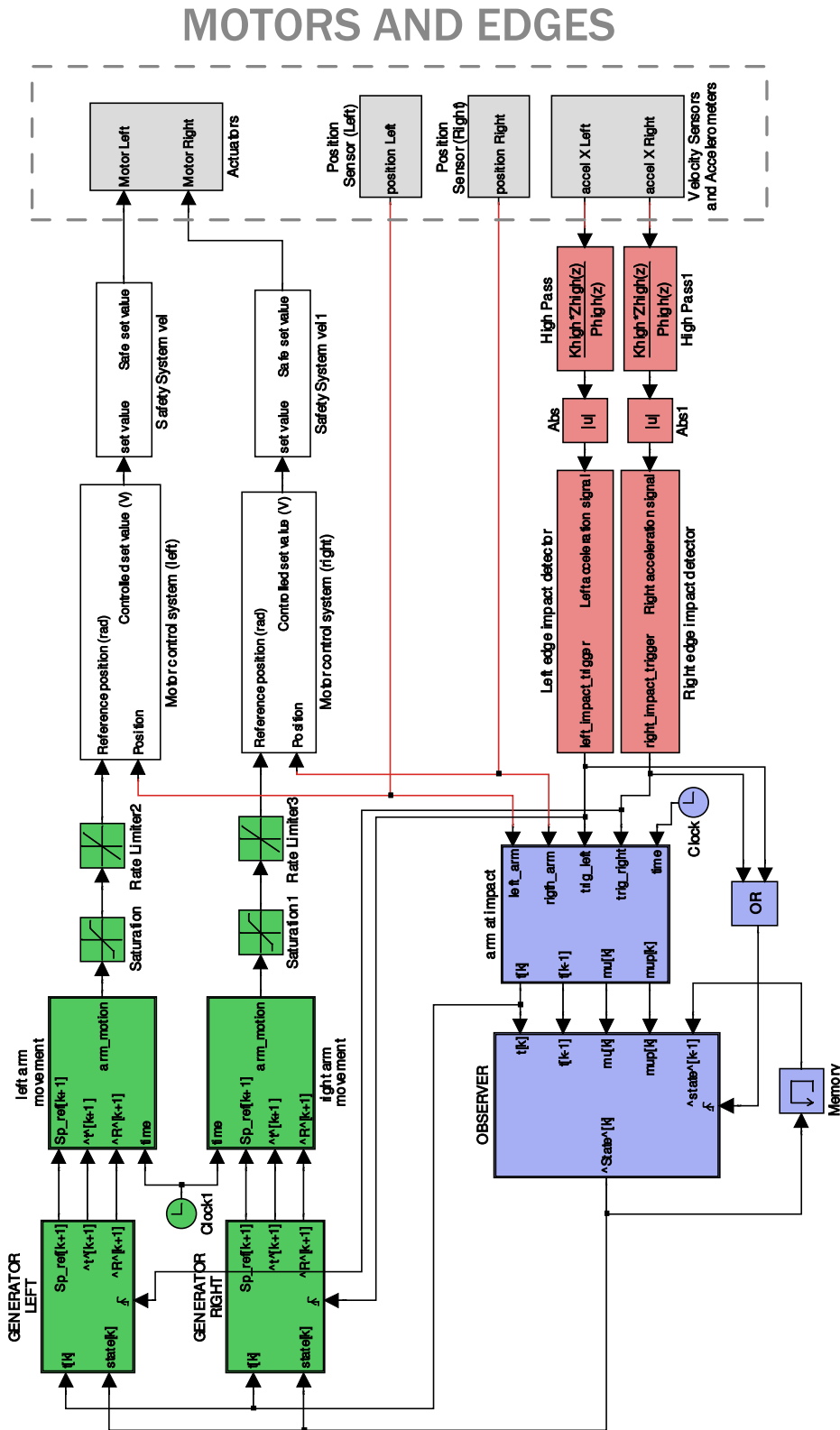Figure B.7: Block diagram (Simulink) of the closed-loop controller.

requested tempo of the periodic cycles to stabilize for the subjects.

We still used XPCTARGET (The Mathworks Inc., Natick, MA), under the target/host computer configuration previously mentioned, to generate the metronome signal and to synchronize the external acquisition devices. The algorithm sampling frequency was 1kHz (1ms as sampling interval).

Appendix C

Computation of Gaze Orientation Under Unrestrained Head Movements

> The soul that can speak through the eyes, can also kiss with a gaze.
>
> Gustav Adolfo Becquer

The present appendix describes the computational technique we used to calculate the gaze orientation of human subjects in the data reported in Chapter 8.

C.1 Introduction

The accurate measurement of eye movements is crucial to oculomotor research. These movements are commonly expressed in terms of their horizontal, vertical, and torsional components, assuming a ball-in-socket model for the eye with three degrees of freedom (DOF). There is an enormous body of literature investigating eye movements under the head fixed condition, and describing accurate methods of measuring these rotations. Such methods are mainly based on either the *dual search coil technique* (Robinson, 1963; Collewijn et al., 1985) or *video image processing* devices (e.g. Nakayama, 1974; Haslwanter, 1995; Moore et al., 1996). Both coil- and video-based techniques are widely used by the oculomotor community in behavioral and clinical studies (e.g. Orban de Xivry et al., 2006; Yuksel et al., 2005).

The dual search coil technique is based on the measurement of electric fields induced in a coil placed directly on the subject's eye. The intensity of the electric field in the coil depends on the orientation of the coil (i.e., of the eye) with respect to an alternating magnetic field. Video image processing devices are designed to measure eye movements with camera-based systems. These techniques are more difficult to

apply, however, when gaze orientation arises from a combination of head and eye movements. Video-based systems are usually based on processing images from a camera fixed to the head. It follows that they do not capture any head movement, but only the eye-in-head component of gaze orientation. The coil technique captures the true eye-in-space orientation, on the other hand, but cannot cope with *translations* of the head since the magnetic field in the recording chamber is supposed to be uniform. In addition, *rotations* of the head always induce a translation of the eye center that is not captured by search coil algorithms. This induces a non-linear bias in the computed signals.

In the study described in this appendix, we measure the eye-in-head and head-in-space positions independently. Our technique is therefore valid for very large head movements, or even displacements of the body. Using the coil technique with an unrestrained head would require the measurement of head position, and the integration of this information using an algorithm similar to that presented in this appendix. This study provides a robust geometrical basis for computing the gaze orientation with no restrictions on head movement.

The mathematical developments of this appendix are based on common linear algebra operations. Head rotations are represented as a 3x3 matrix, according to the well-known sequence of Fick angles (Fick, 1874; Haslwanter, 1995), and head translations as a 3x1 position vector. The combination of head position and orientation, hereafter referred to as the head *pose*, therefore has 6 DOF. The eye-in-head orientation is similarly represented by a 3x3 matrix with 3 DOF, since the center of the eye is assumed to be fixed with respect to the head. Similar formalisms have been used by Allison et al. (1996) in testing the vestibular system, and by Wang and Sung (2002) to estimate gaze orientation in front of a computer screen. These translations and rotations could be represented in other ways, e.g. dual-number quaternions. There are even some papers dedicated to comparing these methods, originally from the perspective of robot kinematics (e.g. the survey by Aspragathos and Dimitros, 1998) and later with respect to the computation of eye rotations (Tweed et al., 1990; Haslwanter, 1995). Note that for the sake of simplicity this appendix does not take into account eye-in-head *torsion*, which corresponds to the third Fick angle and captures eye rotation around the optical axis. This angle can be measured by both search coil (e.g. Tweed et al., 1990) and video-based devices (e.g. Moore et al., 1996), however, and can easily be integrated into the eye-in-head orientation matrix. Eye torsion does not change the line of sight.

This appendix also addresses the issue of calibration. We present an efficient calibration protocol based on gaze fixation during self-paced, smooth head movements. This protocol can be easily adapted to a broad range of environments, since it only requires knowing the location of the fixation target in a 3D, ground-based coordinate system.

We will particularly stress the algorithmic sequence followed in computing gaze orientation from the head-in-space and eye-in-head components, via translations and rotations that are simply described using linear algebra. The method is therefore

simple, robust, and computationally efficient. Its main hardware requirement is a
device that can measure the position of three points on the subject's head in a
ground-based coordinate system. This appendix also describes experimental results
validating our algorithm, obtained by using a video-based device to measure the
eye-in-head position. The method essentially consists of two steps:

1. determining the eye orientation in the head coordinate system; and

2. rotating the eye orientation vector into a ground-based coordinate system,
   using information on the head orientation provided by the head measurement
   device.

The rest of this appendix is organized as follows. The "Materials and Meth-
ods" section (C.2.1) describes the geometrical relationships required to compute the
eye-in-head and head components of gaze, and describes their mutual interaction.
Section C.2.2 discusses the calibration required to integrate measurements from both
acquisition devices. Section C.2.3 describes the validation tasks. The results of val-
idation are summarized in Section C.3, and the characteristics of this new method
are discussed in Section C.4.

C.2 Materials and Methods

C.2.1 Geometrical developments

A geometric basis for measurement of eye position under the head fixed condition
have been derived by Moore et al. (1996). The center of the eye is assumed to be fixed
with respect to the head throughout the task. This section explains how Moore's
method can be extended to unrestrained head conditions, when the subject's head
is free to move without constraint. This technique provides *separate* signals for the
head and eye orientations, and therefore distinguishes the relative contributions of
each component to gaze orientation.

Gaze is treated as a vector in space, with its origin at the eye center and its
direction following from both the head's orientation in space and the eye's orien-
tation in the head. According to this method, gaze orientation has to be derived
independently for each eye. This appendix therefore focuses on derivations involving
one eye, except for a short section dedicated to the calculation of vergence (in Sec-
tion C.2.1). In the following discussion, matrices are represented by bold uppercase
characters (e.g. $\mathbf{R}$), vectors and points in 3D space by normal uppercase characters
(e.g. P), and scalar quantities by lowercase italic characters (e.g. x).
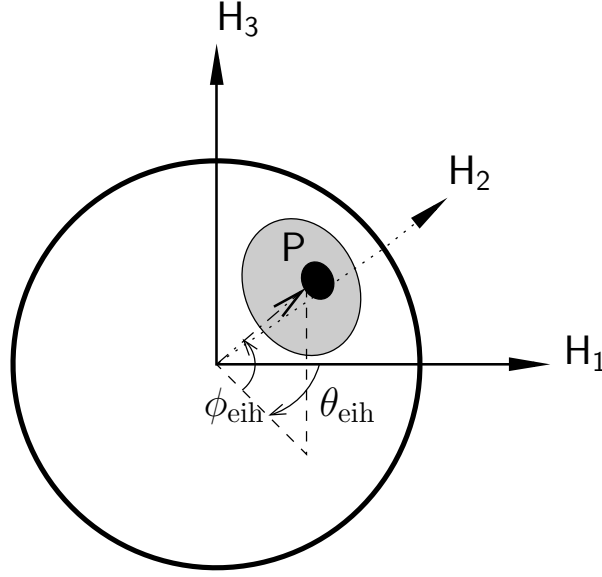
Figure C.1: Diagram of the eye's orientation in the head coordinate system $[\mathsf{H}_1, \mathsf{H}_2, \mathsf{H}_3]$. P denotes the pupil center, and $(\theta_{\mathrm{eih}}, \phi_{\mathrm{eih}})$ are the horizontal and vertical Fick angles of the eye's orientation.

Eye position through image processing

According to Moore et al. (1996), the vertical and horizontal Fick angles of eye-in-head orientation as measured by a video-based device are given by

$$\phi_{\mathrm{eih}} = \arcsin\left(-a'_{21}x - a'_{22}y - a'_{23}\right) \tag{C.1}$$

$$\theta_{\mathrm{eih}} = \arcsin\left(\frac{a'_{11}x + a'_{12}y + a'_{13}}{\cos\left(\phi_{\mathrm{eih}}\right)}\right), \tag{C.2}$$

where the coefficients ('gains') a'_{ij} are determined by calibration (see Section C.2.2) and (x, y) are the coordinates of the pupil's center in the camera image. Both angles are depicted in Fig. C.1.

The main geometrical developments of Moore et al. (1996) are summarized in Appendix C.A of this chapter. The eye orientation *vector* in the head coordinate system follows directly from (C.27).

Head pose through image processing

Head pose is defined in terms of a *ground-based* (i.e., motionless with respect to the laboratory) coordinate system $[\mathsf{G}_1, \mathsf{G}_2, \mathsf{G}_3]$ (see Fig. C.2). To efficiently compute the head pose one must measure the position of three points on the head, which must not be collinear. Let us denote these points by T_a, T_b and T_c. They are represented by grey dots in Fig.s C.2 and C.6, and define a plane parallel to the

frontal plane $H_2 - H_3$. Since the head is assumed to be a rigid body, the position
of these points completely determines the head pose. It is of particular interest to
determine the position of the eye center, i.e., the origin of the gaze. We assume that
the position of this point can be deduced from the positions of $T_{\{a,b,c\}}$ and prior
knowledge of the head's anthropomorphic characteristics. The position of the eye
center, $E = (e_1, e_2, e_3)^T$, is taken as the origin of the $[H_1, H_2, H_3]$ coordinate system
as depicted in Fig. C.2.

The head orientation is defined as the orientation of the vector H_1 with respect
to the coordinate system $[G_1, G_2, G_3]$. This unit vector is computed using the cross
product (hereafter denoted by $\times$) of two vectors between different pairs of points in
$T_{\{a,b,c\}}$, e.g.

$$H_1 = \frac{(T_c - T_a) \times (T_b - T_a)}{|(T_c - T_a) \times (T_b - T_a)|}. \tag{C.3}$$

The head orientation angles follow from this vector in a straightforward manner:

$$\theta_{\mathrm{h}} = \arctan\left(\frac{h_{12}}{h_{11}}\right) \tag{C.4}$$

$$\phi_{\mathrm{h}} = -\arcsin(h_{13}), \tag{C.5}$$

where $(h_{11}, h_{12}, h_{13})^T = H_1$.

The torsional component of the head orientation must also be computed. This
does not influence the line of sight, but it does modify the relationship between
the eye-in-head $[H_1, H_2, H_3]$ and ground-based $[G_1, G_2, G_3]$ coordinate systems. The
head rotation must be computed to know how the two gaze components should be
combined. The head axis H_1 is made parallel to G_1 by left-multiplying the vectors
T with the following orthogonal rotation matrix:

$$
\begin{pmatrix}
\cos(\theta_{\mathrm{h}})\cos(\phi_{\mathrm{h}}) & -\sin(\theta_{\mathrm{h}}) & \cos(\theta_{\mathrm{h}})\sin(\phi_{\mathrm{h}}) \\
\sin(\theta_{\mathrm{h}})\cos(\phi_{\mathrm{h}}) & \cos(\theta_{\mathrm{h}}) & \sin(\theta_{\mathrm{h}})\sin(\phi_{\mathrm{h}}) \\
-\sin(\phi_{\mathrm{h}}) & 0 & \cos(\phi_{\mathrm{h}})
\end{pmatrix}^{-1}
$$

$$
=
\begin{pmatrix}
\cos(\theta_{\mathrm{h}})\cos(\phi_{\mathrm{h}}) & -\sin(\theta_{\mathrm{h}}) & \cos(\theta_{\mathrm{h}})\sin(\phi_{\mathrm{h}}) \\
\sin(\theta_{\mathrm{h}})\cos(\phi_{\mathrm{h}}) & \cos(\theta_{\mathrm{h}}) & \sin(\theta_{\mathrm{h}})\sin(\phi_{\mathrm{h}}) \\
-\sin(\phi_{\mathrm{h}}) & 0 & \cos(\phi_{\mathrm{h}})
\end{pmatrix}^{T}
\tag{C.6}
$$

Geometrically, head torsion corresponds to the angle between this rotated vector
$(T_c - T_b)$, hereafter referred to as the *forehead* vector $F = (f_1, f_2, f_3)^T$, and the G_2
axis. This angle is equal to

$$\psi_{\mathrm{h}} = \arctan\left(\frac{\cos(\theta_{\mathrm{h}})\sin(\phi_{\mathrm{h}})f_1 + \sin(\theta_{\mathrm{h}})\sin(\phi_{\mathrm{h}})f_2 + \cos(\phi_{\mathrm{h}})f_3}{-\sin(\theta_{\mathrm{h}})f_1 + \cos(\theta_{\mathrm{h}})f_2}\right). \tag{C.7}$$

The gaze in space

This section integrates the previously defined eye-in-head and head components of
the gaze orientation into a single vector giving the gaze orientation in the $[G_1, G_2, G_3]$
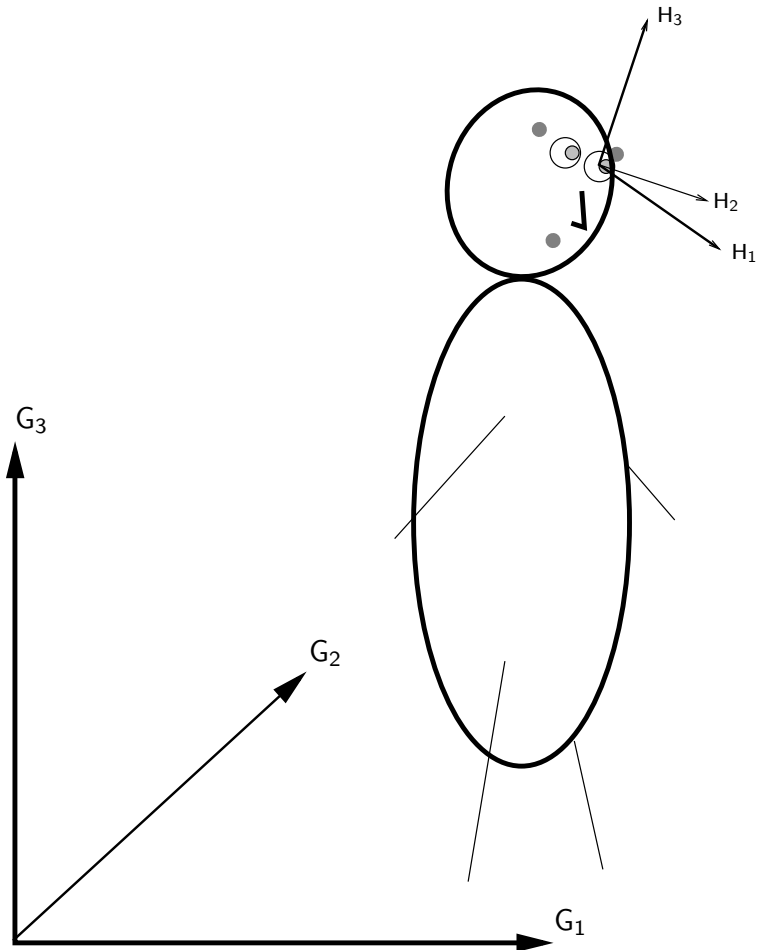
Figure C.2: Diagram of the whole body. This figure emphasizes the components of the gaze orientation: the head component is due to the head pose in the ground-based coordinate system $[\mathsf{G}_1, \mathsf{G}_2, \mathsf{G}_3]$, and the eye-in-head component is due to the eye's orientation in the head coordinate system $[\mathsf{H}_1, \mathsf{H}_2, \mathsf{H}_3]$. The grey dots denote the points T_a, T_b and T_c (see Fig. C.6 for more details), which are measured to determine the head pose.

coordinate system. The origin of this vector is the center of the eye E. The orientation vector follows directly from the eye-in-head vector P, and can be obtained by substituting (C.1) and (C.2) into (C.27), then applying three rotations to the result: first by the horizontal angle θ_h, then by the "meridian" angle ϕ_h, and finally by the torsional angle ψ_h obtained from (C.4), (C.5) and (C.7) respectively:

$$
\begin{aligned}
P_G &= \begin{pmatrix} \cos(\theta_h) & -\sin(\theta_h) & 0 \\ \sin(\theta_h) & \cos(\theta_h) & 0 \\ 0 & 0 & 1 \end{pmatrix} \begin{pmatrix} \cos(\phi_h) & 0 & \sin(\phi_h) \\ 0 & 1 & 0 \\ -\sin(\phi_h) & 0 & \cos(\phi_h) \end{pmatrix} \begin{pmatrix} 1 & 0 & 0 \\ 0 & \cos(\psi_h) & -\sin(\psi_h) \\ 0 & \sin(\psi_h) & \cos(\psi_h) \end{pmatrix} P \\
&= \begin{pmatrix} \cos(\theta_h)\cos(\phi_h) & \cos(\theta_h)\sin(\phi_h)\sin(\psi_h)-\sin(\theta_h)\cos(\psi_h) & \cos(\theta_h)\sin(\phi_h)\cos(\psi_h)+\sin(\theta_h)\sin(\psi_h) \\ \sin(\theta_h)\cos(\phi_h) & \sin(\theta_h)\sin(\phi_h)\sin(\psi_h)+\cos(\theta_h)\cos(\psi_h) & \sin(\theta_h)\sin(\phi_h)\cos(\psi_h)-\cos(\theta_h)\sin(\psi_h) \\ -\sin(\phi_h) & \cos(\phi_h)\sin(\psi_h) & \cos(\phi_h)\cos(\psi_h) \end{pmatrix} P \\
&= R_h P
\end{aligned}
\tag{C.8}
$$

P_G therefore denotes the vector from E to P in the ground-based coordinate system, and defines the orientation of the line of sight.

Vergence

In general, the lines of sight of both eyes intersect at a specific distance from the subject called the depth of focus. The angle defining the difference between the two lines of sight is called the *vergence*. This point of intersection is easily determined with our method, since the origins (E_l and E_r, for the left and right eyes respectively) and directions (P_{Gl} and P_{Gr}) of both lines are known. While the two lines of sight should belong to a common plane, measurement noise may skew their apparent orientations. In this case, the best approximation to their point of intersection is halfway along the segment connecting their two closest points[1]. This point, denoted P_{Gv}, is equal to (Goldman, 1990)

$$
P_{Gv} = \frac{(E_l + P_{Gl}s_l + E_r + P_{Gr}s_r)}{2},
\tag{C.9}
$$

where s_l and s_r are given by

$$
s_l = \frac{\det(E_r - E_l, P_{Gr}, P_{Gl} \times P_{Gr})}{|P_{Gl} \times P_{Gr}|^2}
\tag{C.10}
$$

$$
s_r = \frac{\det(E_r - E_l, P_{Gl}, P_{Gl} \times P_{Gr})}{|P_{Gl} \times P_{Gr}|^2}.
\tag{C.11}
$$

P_{Gv} can therefore be interpreted as the subject's point of interest.

---

[1]Geometrically, this segment is *orthogonal* to both lines of sight.

Summary of the procedure

After calibration (see Section C.2.2) it is possible to compute the angular orientation of the eye in space, given the position of the pupil center $(x, y)^T$ in the head coordinate system and the positions of the points T, as follows:

(i) The head orientation angles θ_h, ϕ_h, and ψ_h are computed from the positions of T_a, T_b and T_c using Equations (C.4), (C.5) and (C.7).

(ii) The position of the eye center E is computed from the positions of T_a, T_b and T_c and known anthropomorphic parameters.

(iii) Vertical and horizontal eye angles are computed from (C.1) and (C.2), using coefficients determined through calibration.

(iv) The eye-in-head orientation vector P is then determined from these angles and (C.27).

(v) The eye orientation vector is expressed in terms of the ground coordinate system by applying the rotation matrix (C.8).

(vi) Optionally, the eye-in-space horizontal and vertical Fick angles of the gaze are computed by the equations

$$\theta_\mathrm{G} \;=\; \arctan\left(\frac{p_{G2}}{p_{G1}}\right) \tag{C.12}$$

$$\phi_\mathrm{G} \;=\; -\arcsin\left(p_{G3}\right), \tag{C.13}$$

where $(p_{G1}, p_{G2}, p_{G3})^T = \mathsf{P_G}$.

(vii) The point of intersection between the lines of sight and the angle of vergence can also be computed, according to the equations derived in the corresponding section.

C.2.2   Calibration method

As addressed earlier, the points T fixed to the head are assumed to be measured in the ground-based coordinate system. We also assume that they define a plane parallel to the frontal plane, such that $\theta_\mathrm{h} = \phi_\mathrm{h} = \psi_\mathrm{h} = 0$ when the subject is looking straight ahead (the primary position). If the points T cannot be accurately fixed with respect to the subject's head, they can still be calibrated to ensure that $\theta_\mathrm{h} = \phi_\mathrm{h} = \psi_\mathrm{h} = 0$ in the primary position by a method outlined in Appendix C.B of this chapter.

Calibration protocols for the measurement of eye-in-head orientation via pupil detection by image processing devices are well documented in the literature (e.g. Haslwanter and Moore, 1995; Moore et al., 1996; Clarke et al., 2002; Schreiber and

Haslwanter, 2004). They are generally based on a small number of fixations at *known* horizontal and vertical Fick angles in the head coordinate system. The objective of calibration is to identify the unknown coefficients a'_{ij} in (C.1) and (C.2). The torsional component does not need to be calibrated for image processing devices, since the polar cross-correlation technique provides an angular measurement directly. It is only necessary to define an iral reference signature indicating the eye's primary position in the orbit.

This appendix considers tasks in a framework where the head is unrestrained, and it is inconvenient to ask a subject to keep their head fixed during calibration. The identification of fixation targets at known horizontal and vertical positions with respect to the head coordinate system is therefore impractical. To cope with these restrictions, we propose a calibration protocol that integrates the head pose measurement. The subject is asked to move their head while keeping their gaze fixed on a specific point. The results of the calibration have to match the eye displacements generated by this procedure, given the horizontal and vertical Fick angles of the target in the head coordinate system $[\mathsf{H}_1, \mathsf{H}_2, \mathsf{H}_3]$ (Fig. C.2).

In the head coordinate system, the Fick angles of the fixation target C vary with head position as follows:

$$\theta_{\text{tar}} = \arctan\left(\frac{c_{f_2}}{c_{f_1}}\right) \tag{C.14}$$

$$\phi_{\text{tar}} = -\arcsin\left(c_{f_3}\right), \tag{C.15}$$

where

$$(c_{f_1}, c_{f_2}, c_{f_3})^T = \mathsf{C_f} = \mathbf{R}_{\text{h}}^T(\mathsf{C} - \mathsf{E}) \tag{C.16}$$

is the position of C in the head coordinate system whose origin is the eye center. The calibration is performed by inverting (C.1) and (C.2), and adding a third equation that represents the translation offset (see Maxwell, 1951; Denavit and Hartenberg, 1955, for references about general homogeneous coordinates):

$$\begin{pmatrix} \sin\left(\theta_{\text{tar}}\right)\cos\left(\phi_{\text{tar}}\right) \\ -\sin\left(\phi_{\text{tar}}\right) \\ 1 \end{pmatrix} = \mathbf{A} \begin{pmatrix} x \\ y \\ 1 \end{pmatrix} = \begin{pmatrix} a'_{11} & a'_{12} & a'_{13} \\ a'_{21} & a'_{22} & a'_{23} \\ a'_{31} & a'_{32} & a'_{33} \end{pmatrix} \begin{pmatrix} x \\ y \\ 1 \end{pmatrix}. \tag{C.17}$$

The best "gain" matrix $\mathbf{A}$ for this overdetermined system can be determined by any numerical processing software. The computation gives the best-fitting solution matrix, in the least squares sense, to the series of eye signals $(x, y, 1)^T$ and target signals $(\sin\left(\theta_{\text{tar}}\right)\cos\left(\phi_{\text{tar}}\right), -\sin\left(\phi_{\text{tar}}\right), 1)^T$ generated by the head movements. This problem is well-conditioned, since the horizontal and vertical eye positions generated during the calibration task are highly independent. The gains a'_{31} and a'_{32} are identified to 0, and a'_{33} to 1, to agree with the form of the vectors used in (C.17).

The subjects we tested reported no difficulty in maintaining gaze fixation during the calibration task, since the velocity of their head displacements was only about 25 deg/s on average. In this range the gain of smooth pursuit is very close to 1

with negligible phase lag (see Lisberger et al., 1981), validating the accuracy of gaze fixation for the expected behavior.

Summary of the procedure To calibrate the eye-in-head orientation with a video-based unit, the subject is asked to maintain gaze fixation on a known point (C) while moving their head first horizontally and then vertically. A series of pupil center displacements $(x, y)^T$ and head pose movements are thereby generated. The gain matrix $\mathbf{A}$ is obtained through the following procedure:

(i) If necessary, the points T are artificially corrected such that $\theta_h = \phi_h = \psi_h = 0$ in the primary position by asking the subject to maintain this position for a few seconds. This procedure is detailed in Appendix C.B.

(ii) The head Fick angles θ_h, ϕ_h and ψ_h are calculated from the T positions and Equations (C.4), (C.5) and (C.7).

(iii) The position of the eye center E is computed from the positions of T_a, T_b and T_c and known anthropomorphic parameters.

(iv) The target position in the head coordinate system is computed from (C.16).

(v) The Fick angles of the target in the head coordinate system are computed by (C.14) and (C.15).

(vi) The components a'_{ij} of (C.17) are calculated, using θ_{tar} and ϕ_{tar} from the previous step and $(x, y)^T$ values from the eye-in-head measurement device.

This calibration method could be easily adapted to clinical studies of patients with oculomotor disorders who are not able to maintain gaze fixation while moving the head. In this case, a "discretized" version of the calibration task could be proposed: for several steady head positions, the patient would be asked to stabilize their gaze toward the calibration target C. Only steady eye-head orientations could be used to compute the linear regression (C.17).

C.2.3   Experimental validation

Data have been collected on 5 human subjects (S1 is female, and S2-S5 are male) between 24 and 27 years of age (mean 25.4). They provided informed written consent, and reported no history of neurological or musculoskeletal disorder. All had normal vision, either natural or corrected. All but one subject was naive regarding the goals of the experiment. All the procedures conducted were approved by the local ethics committee, in compliance with the Helsinki declaration.

A sketch of the experimental setup is given in Fig. C.3. Initially, the subject was asked to stand upon a cross marked on the ground (point A). He or she had to keep their gaze fixed on an IRED marker (point C) placed on a camera tripod 1.3 m away.
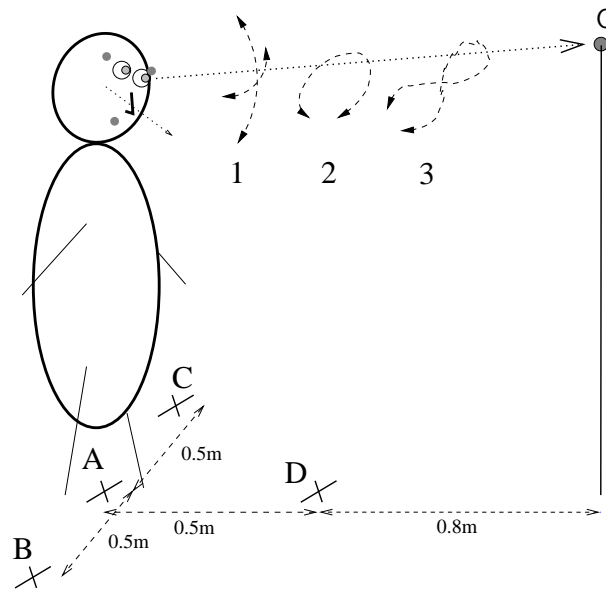
Figure C.3: Experimental setup. Standing on one of the fixed positions (crosses
A, B, C and D), the subject is asked to maintain gaze fixation on the grey spot
(point C) while moving their head in a cross pattern (1), a circular pattern (2), or
an ∞-shaped pattern (3).

Following the method described in Section C.2.2, each subject was asked to move
their head first with a pure horizontal movement, then with a pure vertical movement
(Pattern 1 on Fig. C.3). Two other patterns were used to *validate* the calibration
so obtained. Pattern 2 consisted of a circular head motion, and was used to validate
the *coupling* between horizontal and vertical components. Pattern 3 consisted of a
∞-shaped head motion, the subject being asked to generate significant head *torsion*.
The robustness of the calibration to lateral displacement was evaluated by asking the
subject to repeat these patterns while standing on positions B and C (0.5 m to the
right and left of point A). The robustness of the calibration to distance was evaluated
by repeating the procedure at position D (0.5 m in front of point A). The task was
easy to perform under all conditions, resulting in unambiguous gaze orientations.
Except for pattern 1 on position A, which was used in calibration, every other
pattern and position was used only to validate the method. The method's accuracy
is determined by comparing the computed gaze orientation to the actual position of
C. The subjects went through the following sequence of patterns: pos. A, pattern
1 (calibration) then patterns 2 and 3; pos. B, patterns 1, 2 and 3; pos. C, patterns
1, 2 and 3; pos. D, patterns 1, 2 and 3; and finally pos. A, pattern 1 once more for
a second calibration.

Two-dimensional (horizontal and vertical) recordings of both eyes were made si-
multaneously using a Chronos head-mounted, video-based eye tracker (Clarke et al.,

2003, CHRONOS VISION GmbH, Berlin, Germany). The calculation of eye positions was based on determination of the pupil center (see Zhu et al., 1999, and references therein). The recording frame rate was 200 Hz. The system is linear in the horizontal and vertical planes for deflections up to $\pm$ 20deg, and has a resolution better than 5′. System noise was measured to be 0.11 deg for the horizontal plane and 0.09 deg for the vertical plane (Clarke et al., 2002, 2003). A bite-bar was mounted on the helmet frame to prevent slippage between the head and the helmet. This bite-bar was not mandatory, however, and could be removed for subject comfort. In this case the calibration task would be performed at regular intervals to compensate for any slippage between the head and the helmet. The second video-based device used was a 3D position measurement system. The positions of infrared light-emitting diodes (IREDs) on the Chronos helmet and at the fixation target (the four grey dots on Fig. C.3) were measured using an OptoTrak 3020 system (Northern Digital, Ontario, Canada). The OptoTrak was mounted on the ceiling about 3m in front of the subject. The positions of the IREDs were rotated so that they could be expressed in a coordinate system with axes parallel to the floor and centered on the fixation target. The axes G's of this ground coordinate system are shown in Fig. C.2. The position of each IRED was sampled with a frequency of 200 Hz and resolution of about 0.1 mm within this working environment. The eye signals and IRED signals were filtered at 48 Hz by a zero-phased digital filter (autoregressive, forward and backward). The Chronos eye tracker and the OptoTrak were synchronized by an external computer. Each pattern was executed over a period of 20 s, and its data recorded in a separate file.

C.3 Results

Experimental results are presented in two separate sections. Section C.3.1 describes the calibration results, and Section C.3.2 validates the calibration matrices using data from the patterns described in Section C.2.3.

C.3.1 Calibration

Calibration of the eye-in-head measurement device relies on the algorithm described in Section C.2.2. It assumes that the eye position E is known perfectly with respect to the points T. To keep the method as simple as possible, we assume that this distance is similar for all subjects. Empirical observations of all the subjects wearing the helmet allow us to estimate the eye positions as

$$\mathsf{E} = \frac{2\mathsf{B_T} + \mathsf{T}_c}{3} - 0.09\mathrm{m}\,\mathsf{H}_1 + 0.01\mathrm{m}\,\mathsf{F} \tag{C.18}$$

for the left eye, and

$$\mathsf{E} = \frac{2\mathsf{B_T} + \mathsf{T}_b}{3} - 0.09\mathrm{m}\,\mathsf{H}_1 - 0.01\mathrm{m}\,\mathsf{F} \tag{C.19}$$

Table C.1: Mean and standard deviation of the error by this calibration method.

		first calibration				second calibration			
		Left eye [deg]		Right eye [deg]		Left eye [deg]		Right eye [deg]	
		mean	SD	mean	SD	mean	SD	mean	SD
S1	θ	0.06	1.16	0.01	0.37	0.06	1.05	-0.01	0.27
	ϕ	0	0.53	0	0.44	0	0.49	0	0.24
S2	θ	0.02	0.48	0	0.38	0.01	0.35	0	0.35
	ϕ	0	0.65	0	0.73	0	0.43	0	0.43
S3	θ	0.02	0.65	0	0.37	0.04	0.75	0	0.52
	ϕ	0	0.45	0	0.59	-0.01	1.32	-0.01	1.38
S4	θ	0.03	0.99	-0.01	0.65	0.01	0.28	-0.01	0.39
	ϕ	0	0.85	0	0.58	0	0.36	0	0.4
S5	θ	0.09	1.72	-0.01	0.96	0.02	0.43	0.01	0.82
	ϕ	0	0.38	-0.01	1.08	-0.01	1.16	0	0.6

for the right eye. In these equations $\mathsf{B_T}$ is the barycenter of the points T (see Appendix C.B), which gives an interocular distance of about 0.07 m. Note that any errors induced by this approximation are corrected to the zeroth and first order by the linear gains in (C.17) during the calibration procedure. A more complicated calibration algorithm could treat these distances as additional unknown parameters to be determined. In this case the calibration would become non-linear, however, and in addition to being less robust would require a more complicated and computationally costly implementation.

To calibrate the helmet unit, the subject executed pattern 1 in position A (see Fig. C.3). From the E position computed by (C.18) or (C.19), the *target* Fick angles are computed according to (C.14) and (C.15). The overall motion is slow enough to assume that the subjects maintained a permanent fixation on the point C. In the calibration data (a 20 s recording) the experimenter manually excluded eye blinks, small saccades, and eye movements outside the detection range to reduce signal distortion in the linear regression (C.17).

The real target angles and eye-in-head angles are compared after calibration in Fig. C.4 (left eye, S2). This diagram emphasizes the sinusoidal motion (alternating pure horizontal and pure vertical movements) of the eye-in-head orientation during the smooth head displacement of the calibration task. Fig. C.4 also illustrates the low frequency of the smooth head movements. The green lines denote the error, i.e., the difference between the target angles and the computed eye-in-head angles. The errors in θ over the test period have an average value of 0.01 deg and a standard deviation of 0.35 deg. For ϕ the average error is 0 deg, and the standard deviation is 0.43 deg. Well-conditioned linear regression of (C.17) gives the following matrix
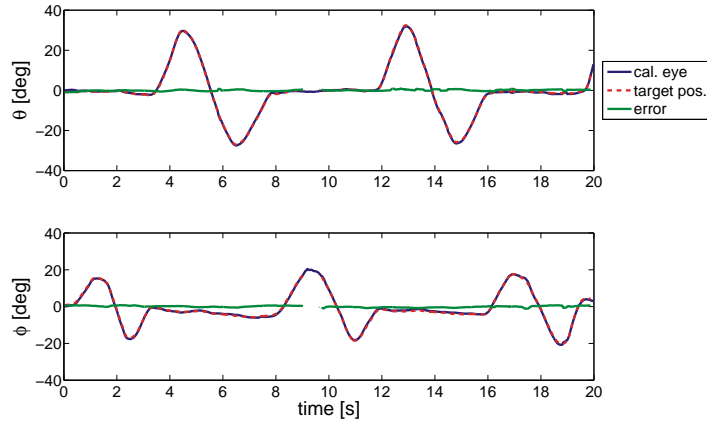
Figure C.4: The target position (dashed red lines) expressed in θ_{tar} (above) and ϕ_{tar} (below) is compared to the computed eye position after calibration (solid blue lines). The solid green lines represent the difference between the two orientations. For eccentric head orientations, in some cases one of the LEDs on the helmet could not be measured (the gaps in the green and red curves around 9s).
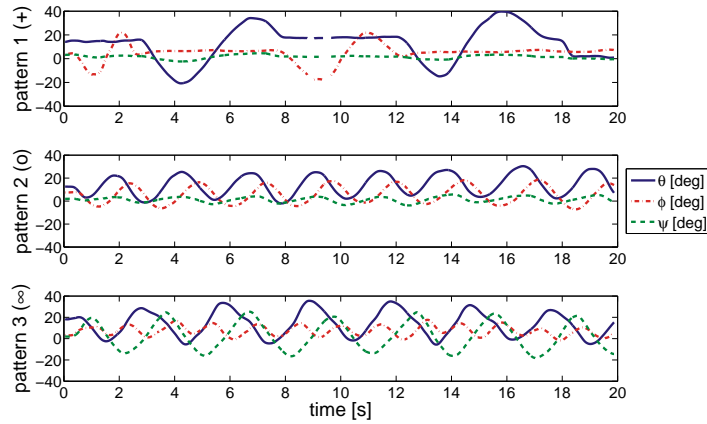
Figure C.5: Typical head motions for the three patterns. Pattern 1 (top) is characterized by alternating pure horizontal (θ, blue solid) and pure vertical (ϕ, red dash-dotted) movements, with no torsion (ψ, green dashed). Pattern 2 (middle) is characterized by coupled, sinusoidal horizontal and vertical movements with a 90 degree phase difference, and limited torsion. In this pattern, the head traces a circle. Pattern 3 (bottom) is characterized by harmonic horizontal and vertical movements in a 2 : 1 frequency ratio (the head follows an ∞-shaped path), and a significant torsion component. For some head orientations, one of the LEDs on the helmet was not measured (the gaps in the curves).

equation for the orientation of the left eye (subject S2):

$$
\begin{pmatrix} \sin\left(\theta_{\text{tar}}\right)\cos\left(\phi_{\text{tar}}\right) \\ -\sin\left(\phi_{\text{tar}}\right) \\ 1 \end{pmatrix} = \begin{pmatrix} 0.0076 & 0.0006 & -0.0005 \\ -0.0002 & 0.0089 & -0.0013 \\ 0 & 0 & 1 \end{pmatrix} \begin{pmatrix} x \\ y \\ 1 \end{pmatrix} \qquad \text{(C.20)}
$$

The average errors and standard deviations of the error, for both eyes and each subject, are listed in Table C.1. The mean error is never significantly different from 0, as should be the case for a linear regression method. The standard deviations, however, certainly reflect a real variability in eye positions (see Ott et al., 1990, and references therein) as well as system noise.

C.3.2   Validation tasks

After performing the calibration task, the subjects were asked to move their heads in other patterns and stand on different predefined points in the workspace. All these tests were to be performed while maintaining their fixation on the same point C (see Section C.2.3). Under these conditions, the known position of C was compared *a posteriori* to the gaze orientation obtained by our algorithm.

Typical head motions for all three patterns are depicted in Fig. C.5. All these data were obtained from subject S2, while standing on point B. The mean value of θ_{h} is therefore positive (the subject's gaze points to the left), while the mean value of ϕ_{h} and ψ_{h} are close to 0 for each pattern. Pattern performances were similar for all subjects, so their validation data were pooled in the analysis.

Several error parameters were computed for each eye, each pattern, and each standing position. $\Delta\theta_{\text{left,right}}$ is the difference between θ_{tar} and the gaze angle θ_{G}; $\Delta\phi_{\text{left,right}}$ is the difference between ϕ_{tar} and the gaze angle ϕ_{G}. We also define the error $\Delta|\alpha_{\text{left,right}}|$ as the absolute value of the angle between the theoretical and the real gaze vectors:

$$
\Delta|\alpha| = \left| \arccos\left(\frac{\mathsf{C_f P_G}}{|\mathsf{C_f}|} \right) \right| \geq 0. \qquad \text{(C.21)}
$$

All these parameters are given in Table C.2, together with the typical ranges of θ_{h}, ϕ_{h}, and ψ_{h} (i.e., the minimum and maximum head angles for each subject).

The average absolute error is always less than 3.5 deg, which is satisfactory with respect to the range of head movements. In particular, the third pattern generates the most important errors. This is due to the relative difficulty of maintaining a fixed gaze while generating the significant head torsion required by this pattern.

As a supplement to this study, several animations of the three patterns have been uploaded to the publisher's web service[2]. They are also available on the first author's web page.

---

[2]URL: `http://www.sciencedirect.com` (Ronsse et al., 2007d)

Table C.2: Error parameters for each standing position {A,B,C,D} and head pattern {1,2,3}. The three first columns present the overall range of head angles for each test. The following angular errors for the left and right eyes are averaged across all subjects: $\Delta\theta_{\mathrm{left}}$ is the difference between θ_{tar} and θ_{G}, $\Delta\phi_{\mathrm{left}}$ is the difference between ϕ_{tar} and ϕ_{G}, and $\Delta|\alpha_{\mathrm{left}}|$ is the total angular error as defined by (C.21). All these data are expressed in degrees (deg). The listed ranges are the standard deviations of the angular errors.

		θ_{h}	ϕ_{h}	ψ_{h}	$\Delta\theta_{\mathrm{left}}$		$\Delta\phi_{\mathrm{left}}$		$\Delta|\alpha_{\mathrm{left}}|$		$\Delta\theta_{\mathrm{right}}$		$\Delta\phi_{\mathrm{right}}$		$\Delta|\alpha_{\mathrm{right}}|$	
					mean	SD	mean	SD	mean	SD	mean	SD	mean	SD	mean	SD
A	P1	±35	±24	±4	−0.06	0.75	0.02	0.62	0.83	0.52	−0.02	0.58	0.03	0.61	0.72	0.44
	P2	±28	±24	±7	0.83	1.64	0.52	1.8	2.26	1.33	0.27	1.14	0.71	1	1.5	0.79
	P3	±36	±23	±30	0.6	1.69	−0.64	1.78	2.35	1.11	0.09	1.5	−0.5	1.71	2.02	1.17
B	P1	−22, 47	±22	±4	0.45	3.47	−0.36	1.08	1.69	3.23	−0.59	1.18	−0.03	0.86	1.32	0.86
	P2	−17, 41	±24	±9	0.23	1.09	−0.33	1.01	1.2	0.96	−0.35	1.28	−0.35	0.88	0.97	1.25
	P3	−37, 46	±22	±30	0.06	3.47	−0.5	1.56	1.61	3.47	−0.45	1.26	−0.64	1.48	1.72	1.18
C	P1	−50, 23	±24	±4	−0.45	0.99	−0.25	1.37	1.43	1.05	−0.58	1.07	−0.12	1.51	1.61	1.09
	P2	−37, 16	±23	±9	−0.31	1.2	−1.23	1.43	1.98	1.08	−0.45	1.1	−0.85	1.55	1.91	0.95
	P3	−53, 23	±25	±33	−0.12	1.16	−1.15	1.44	1.95	0.98	0.05	1.45	−1.21	1.6	2.22	1.09
D	P1	±35	±20	±4	0.11	0.82	0.4	0.88	1.04	0.72	0.37	0.78	0.45	0.84	1.08	0.69
	P2	±29	±25	±7	0.56	0.91	0.72	1.16	1.59	0.71	0.76	0.66	0.73	1.39	1.75	0.66
	P3	±34	±21	±32	0.49	0.98	1.03	1.54	1.96	0.88	0.81	1.02	0.41	1.35	1.77	0.75
A	P1	±36	±24	±4	0.07	2.31	0.03	0.91	0.76	2.33	−0.04	0.48	0.01	0.62	0.58	0.52

C.4 Discussion

This appendix investigates the geometry of human gaze orientations. To compute gaze orientation in a behavioral context where the head has complete freedom of movement, not only head rotations but also head *translations* must be taken into account. This appendix provides a simple calibration protocol that can integrate both eye-in-head and head-in-space orientations into a single coordinate system.

Our method rests on separate measurements of the head pose and the eye-in-head position. The head pose is determined by measuring the positions of three markers fixed to the head. In the present experiment the eye-in-head position is recorded with a video-based device, but any other classical eye recording method (corneal reflection methods, EOG, etc.) will do as well. The availability of independent head and eye-in-head orientation signals invites further investigation of their interaction. For example, if a search coil is used then eye-in-space angular components are recorded directly but a contribution due to head motion must be subtracted from this signal (see e.g. Crawford and Vilis, 1991; Crawford et al., 1999, 2003; Harris et al., 2001; Han et al., 2005).

Dual search coil and video-based devices are equally popular methods of measuring eye orientation, and each has its specific advantages and drawbacks. On the one hand, *dual search coils* (Robinson, 1963; Collewijn et al., 1985) are expensive and fragile. They are also invasive, since a human subject can endure the presence of a coil on their eye for at most 40 minutes, and require the supervision of an ophthalmologist. Moreover, because the coil measures eye orientation in a ground-based coordinate system it is not straightforward to isolate the eye-in-head component of the gaze orientation. The main advantages of the search coil technique are its excellent spatial accuracy and the high sampling frequencies that can be obtained. With horizontal, vertical, and torsional gaze orientations available in real time, it is easy to implement closed-loop protocols. On the other hand, recent *video image processing* devices have been able to accurately measure eye movements using camera-based systems (see the paper by Clarke et al., 2003, that presents the device used in this study). These techniques are currently approaching the search coil technique in terms of spatial and temporal accuracy. Most importantly, they are much less invasive.

With the development of more advanced hardware, a mathematical formalism based on 3D rotations has been established to relate facial images to gaze orientation (Nakayama, 1974; Tweed and Vilis, 1987; Tweed et al., 1990; Van Opstal, 1993; Haslwanter, 1995). Horizontal and vertical displacements of the eye are computed by tracking the pupil center (see Zhu et al., 1999, and references therein). Torsion may be computed either by tracking natural or artificial landmarks on the eye (Nakayama, 1974; Parker et al., 1985; Ott et al., 1990), or by tracking the iral intensity along a circular sampling path (the *polar cross-correlation* method) (Hatamian and Anderson, 1983; Vieville and Masse, 1987; Tweed et al., 1990; Clarke et al., 1991; Moore et al., 1991; Haslwanter, 1995; Haslwanter and Moore, 1995; Moore

et al., 1996; Haslwanter, 2000; Schreiber and Haslwanter, 2004).

The main limitation of video-based acquisition systems is that they do not capture head motions, since the cameras recording eye motion are fixed to a helmet worn by the subject. This appendix proposes a method of integrating both translations and rotations of the head into any video-based system, based on the measurement of three points on the subject's head. This extra information allows the gaze orientation to be calculated accurately in a ground-based coordinate system. The first part of this appendix (Section C.2.1) covered the geometrical developments of our method. Eye-in-head orientation is first computed using classical techniques (Moore et al., 1996), then translated and rotated into the ground coordinate system once the head pose has been computed. For the sake of simplicity, this appendix did not summarize the existing methods of computing eye *torsion* from video-based devices. Eye torsion does not modify the line of sight, so is not a critical issue within the scope of this appendix.

In addition to the accurate video-based devices described above, we would like to discuss another fruitful aspect of gaze estimation in the literature. Several methods have been developed to estimate the gaze orientation of a head before a computer screen. The goal of such studies is to use gaze as part of the interface between humans and computerized devices, for applications both clinical and otherwise. The main difference between these methods and the technique described in this appendix lies in the hardware; the cameras that track the eye pupil must be fixed to a ground-based coordinate system instead of the subject's head. This has the advantage of measuring gaze orientation directly in the ground-based coordinate system. On the other hand, it also requires continuous monitoring of the distance between the camera and the eye, which is not easy to measure accurately. Even though the most recent of these methods take head translations into account, they cannot compute gaze orientation for very large head displacements (for example, about 1m). Furthermore, these techniques do not achieve the level of spatial and temporal resolution required in oculomotor research. Papers of interest in this field of study include that of Newman et al. (2000), which proposes a method of reconstructing the head pose in real time (30Hz) by tracking typical features of the head; and that of Wang and Sung (2002), which presents a similar method based on linear algebra with homogeneous coordinates. An overview of this topic can be found in recent papers (Shih and Liu, 2004; Yoo and Chung, 2005), as well as the "Computer Vision Bibliography" web page which refers extensively to this literature[3]. Finally, an alternative approach to determining the point of gaze has been developed by Yu and Eizenman (2004). This method is based on the detection of corresponding points in an image from a head-mounted scene camera and a reference image. This method is not designed to accurately locate the head and other objects in a 3D ground-based coordinate system.

In contrast with the restricted workspace of a computer screen, our method

---

[3]`http://iris.usc.edu/Vision-Notes/bibliography/people911.html`

allows not only large head movements but also subject displacements as long as the head markers T remain in the recording space.

In Section C.2.2, we detailed an algorithm for calibrating a video-based eye tracker unit by converting pixel outputs into angular displacements. The mathematical operations involved in this calibration rest on the rotation and translation of vectors and matrices, as was the case for computation of the gaze orientation.

The main advantages of our method can be summarized as follows:

- it is non-invasive for the subjects, since a video-based device is used to compute eye-in-head orientation;

- its algorithm is expressed in terms of linear algebra, and is therefore computationally efficient;

- it separates the eye-in-head and the head-in-space components of gaze, thus allowing the study of their mutual interaction;

- it can be used with a wide variety of acquisition devices, provided that the 3D positions of three points on the head can be independently measured;

- it is based on the geometry of the body, so is easy to understand and implement;

- it is robust under challenging experimental conditions; a preliminary version of this method has already been tested in parabolic flight campaigns by the European Space Agency.

Future improvements to our method mainly concern algorithmic issues: nonlinear estimation of the eye center position with respect to the head markers (this would, however, greatly complicate the calibration algorithm), more accurate pupil center detection (see Zhu et al., 1999), decoupling the horizontal and vertical axes of eye rotation (Schreiber and Haslwanter, 2004), etc.

Section C.3 was devoted to the experimental validation of our method. The calibration process has been strongly validated by data from five different human subjects, confirming that the proposed linear algorithm accurately reflects the dynamics of gaze orientation. Using the calibration matrices so obtained, we also performed other validation tasks. As expected, the smallest angular errors were measured for the first pattern in position A; i.e., for the data using in computing the calibration matrix. The errors remained within reasonable bounds, however, for all head patterns and standing positions. In general, the angular errors obtained in the validation tasks compared favorably to the natural variability of gaze orientation in typical fixation tasks (see Ott et al., 1990, and references therein). The errors incurred by this method are also similar to those obtained by previous experiments comparing the accuracy of video-based and search coil eye tracking techniques in human experiments (e.g. Ott et al., 1990; Moore et al., 1996; Clarke et al., 2002, 2003).
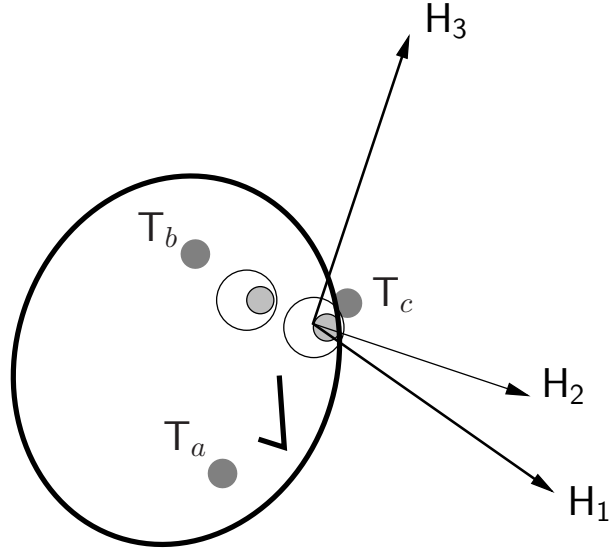
Figure C.6: Diagram of the head in space. The coordinate system $[\mathsf{H}_1, \mathsf{H}_2, \mathsf{H}_3]$ is fixed to the head, with its origin at the center of the (arbitrarily chosen) left eye. This point is also the origin of the gaze orientation vector. The points $\mathsf{T}_{\{a,b,c\}}$ are fixed on the head, and discussed in Section C.2.1.

This appendix therefore provides a computationally efficient procedure for computing eye orientation in a ground-based coordinate system. This method can be implemented rapidly in a variety of settings, since it is based on linear transformations related to the actual body configuration. This material has been published as such in Ronsse et al. (2007d).

C.A   Eye-in-head orientation

We define an orthogonal, right-handed, head-based coordinate system $[\mathsf{H}_1, \mathsf{H}_2, \mathsf{H}_3]$ with its origin at the center of the eyeball. The H_2 axis is parallel to the interaural axis, and the $\mathsf{H}_2 - \mathsf{H}_3$ plane is parallel to the frontal plane. The H_1 axis therefore points out of the face from the occiput (see Fig. C.6). The eye's *primary position* is defined as the position where its line of sight corresponds to the H_1 axis. We also define a *camera* coordinate system $[\mathsf{C}_1, \mathsf{C}_2, \mathsf{C}_3]$, where C_2 and C_3 lie within the image plane and C_1 corresponds to the optical axis of the camera.

According to the definition of Moore et al. (1996), the coordinates of the pupil center with respect to the head coordinate system $\mathsf{P} = (p_1, p_2, p_3)^T$ and the the camera coordinate system $\mathsf{P}' = (p_1', p_2', p_3')^T$ are related by

$$\mathsf{P}' = \mathbf{R}_{\mathrm{cam}}\, \mathsf{P} + \mathsf{T}_{\mathrm{cam}}, \tag{C.22}$$

where $\mathsf{T}_{\mathrm{cam}}$ and $\mathbf{R}_{\mathrm{cam}}$ are the translation vector and rotation matrix relating the

head coordinate system to the camera coordinate system. Angular positions of the
eye are expressed in terms of Fick angles (Fick, 1874; Haslwanter, 1995), which
are commonly used in oculomotor research. If the space around the eye is viewed
as a sphere marked with parallels and meridians, then the sequence of Fick angles
defining an orientation is as follows: first a horizontal rotation θ along the equator,
then a vertical rotation ϕ along a meridian, and finally a torsional rotation ψ about
the optical axis. According to the right-hand rule, eye movements to the left, down,
and clockwise are positive from the subject's point of view.

Moore et al. (1996) showed that the horizontal (θ_{cam}) and vertical (ϕ_{cam}) com-
ponents of the offset matrix $\mathbf{R}_{\mathrm{cam}}$ can be captured by calibration gains and do not
influence the accuracy of measurement if they remain bounded within 5 deg. This
assumption is reasonable, provided the camera is properly fixed to the acquiring
device. Equation (C.22) therefore reduces to

$$\mathsf{P}' = \begin{pmatrix} 1 & 0 & 0 \\ 0 & \cos\left(\psi_{\mathrm{cam}}\right) & -\sin\left(\psi_{\mathrm{cam}}\right) \\ 0 & \sin\left(\psi_{\mathrm{cam}}\right) & \cos\left(\psi_{\mathrm{cam}}\right) \end{pmatrix} \mathsf{P} + \mathsf{T}_{\mathrm{cam}}, \tag{C.23}$$

where ψ_{cam} denotes an offset rotation of the camera around its optical axis.

If the distance between the lens plane and the center of the eye is large compared
to the distance between the lens plane and the image plane of the camera (Nakayama,
1974; Moore et al., 1996), then the projection P'' of P' onto the image plane is given
by

$$\mathsf{P}'' = \begin{pmatrix} 0 \\ x \\ y \end{pmatrix} = k \begin{pmatrix} 0 \\ p_2' \\ p_3' \end{pmatrix} \tag{C.24}$$

where k is a scaling factor related to the image magnification and p_i' are the individual
components of P'. By inverting (C.23) and (C.24), we find the following relation
between the actual eye position P and the pupil center $(x, y)^T$ as measured by the
camera:

$$p_2 \;=\; a_{11}x + a_{12}y + a_{13} \tag{C.25}$$
$$p_3 \;=\; a_{21}x + a_{22}y + a_{23}, \tag{C.26}$$

where the coefficients $a_{11} = a_{22} = \cos\left(\psi_{\mathrm{cam}}\right)/k$, $a_{12} = -a_{21} = \sin\left(\psi_{\mathrm{cam}}\right)/k$, $a_{13} = -\cos\left(\psi_{\mathrm{cam}}\right)t_2 - \sin\left(\psi_{\mathrm{cam}}\right)t_3$, and $a_{23} = \sin\left(\psi_{\mathrm{cam}}\right)t_2 - \cos\left(\psi_{\mathrm{cam}}\right)t_3$ all have to be
determined by an appropriate calibration. The scalar variables p_i (t_i, etc.) denote
the individual components of P ($\mathsf{T}_{\mathrm{cam}}$, etc.) respectively.

The pupil center P follows from applying the Fick rotation ($\theta_{\mathrm{eih}}, \phi_{\mathrm{eih}}$) to the eye's
primary position $(r_p, 0, 0)^T$, where r_p is the distance between the center of the eye
and the center of the pupil.

$$\mathsf{P} = \begin{pmatrix} \cos\left(\theta_{\mathrm{eih}}\right)\cos\left(\phi_{\mathrm{eih}}\right) & -\sin\left(\theta_{\mathrm{eih}}\right) & \cos\left(\theta_{\mathrm{eih}}\right)\sin\left(\phi_{\mathrm{eih}}\right) \\ \sin\left(\theta_{\mathrm{eih}}\right)\cos\left(\phi_{\mathrm{eih}}\right) & \cos\left(\theta_{\mathrm{eih}}\right) & \sin\left(\theta_{\mathrm{eih}}\right)\sin\left(\phi_{\mathrm{eih}}\right) \\ -\sin\left(\phi_{\mathrm{eih}}\right) & 0 & \cos\left(\phi_{\mathrm{eih}}\right) \end{pmatrix} \begin{pmatrix} r_p \\ 0 \\ 0 \end{pmatrix} \tag{C.27}$$

These rotations are depicted in Fig. C.1. Substituting this result into (C.25) and (C.26), we arrive at the eye-in-head orientation:

$$\phi_{\text{eih}} \quad = \quad \arcsin\left(-\frac{a_{21}x + a_{22}y + a_{23}}{r_p}\right) \tag{C.28}$$

$$\theta_{\text{eih}} \quad = \quad \arcsin\left(\frac{a_{11}x + a_{12}y + a_{13}}{r_p \cos\left(\phi_{\text{eih}}\right)}\right) \tag{C.29}$$

This result gives (C.1) and (C.2), which define $a'_{ij} \triangleq a_{ij}/r_p$.

C.B   Calibration of the points T

Our gaze estimation method rests on the fact that the points $\mathsf{T}_{\{a,b,c\}}$ define a plane parallel to the frontal plane $\mathsf{H}_2 - \mathsf{H}_3$ (Fig. C.6), while the forehead vector $\mathsf{F} = (\mathsf{T}_b - \mathsf{T}_c)$ is parallel to H_2. In theory this ensures that $\theta_{\text{h}} = \phi_{\text{h}} = \psi_{\text{h}} = 0$ whenever the subject stands up and looks straight ahead (the primary position). The placement of these points on the subject's head, however, cannot be accurate enough to validate this assumption. Offset yaw (θ_{off}), pitch (ϕ_{off}), and torsion (ψ_{off}) angles must therefore be measured while a subject is maintaining the primary position. This appendix describes a calibration protocol that compensates for these errors by virtually moving the points T.

Prior to the calibration pattern, the subject is asked to maintain the primary position by looking straight ahead while their head orientation angles, i.e. the offset angles, are recorded. In this reference posture, the real points $\mathsf{T}_{\{a,b,c\}}$ are related to the so-called corrected points $\mathsf{T}'_{\{a,b,c\}}$ by the transformation $(\mathsf{T}_a, \mathsf{T}_b, \mathsf{T}_c) = \mathbf{R}_{\text{off}}(\mathsf{T}'_a, \mathsf{T}'_b, \mathsf{T}'_c)$, where $\mathbf{R}_{\text{off}}$ is a rotation matrix with exactly the same structure as $\mathbf{R}_{\text{h}}$ in (C.8). However, this last relation is only valid when the Fick angles of $\mathsf{T}'_{\{a,b,c\}}$ are equal to zero. To put it another way, when the points $\mathsf{T}_{\{a,b,c\}}$ are such that their *measured* Fick angles are equal to zero, we have $(\mathsf{T}'_a, \mathsf{T}'_b, \mathsf{T}'_c) = \mathbf{R}_{-\text{off}}(\mathsf{T}_a, \mathsf{T}_b, \mathsf{T}_c)$. In this case, $\mathbf{R}_{-\text{off}}$ is the Fick rotation matrix with angles $-\theta_{\text{off}}$, $-\phi_{\text{off}}$ and $-\psi_{\text{off}}$. In order to make this relation valid for any head orientation, the sets of points $\mathsf{T}_{\{a,b,c\}}$ and $\mathsf{T}'_{\{a,b,c\}}$ must be pre-multiplied by $\mathbf{R}_{\text{h}}^{-1} = \mathbf{R}_{\text{h}}^T$ ($\mathbf{R}_{\text{h}}$ is an orthogonal rotation matrix):

$$\mathbf{R}_{\text{h}}^T (\mathsf{T}'_a, \mathsf{T}'_b, \mathsf{T}'_c) = \mathbf{R}_{-\text{off}}\mathbf{R}_{\text{h}}^T (\mathsf{T}_a, \mathsf{T}_b, \mathsf{T}_c). \tag{C.30}$$

The new set of head points is therefore

$$(\mathsf{T}'_a, \mathsf{T}'_b, \mathsf{T}'_c) = \mathbf{R}_{\text{h}}\mathbf{R}_{-\text{off}}\mathbf{R}_{\text{h}}^T (\mathsf{T}_a, \mathsf{T}_b, \mathsf{T}_c). \tag{C.31}$$

Finally, for convenience this rotation is applied around the *barycenter* B_{T} of $\mathsf{T}_{\{a,b,c\}}$, $(\mathsf{T}_a + \mathsf{T}_b + \mathsf{T}_c)/3$, which is then conserved.

$$(\mathsf{T}'_a, \mathsf{T}'_b, \mathsf{T}'_c) = \mathbf{R}_{\text{h}}\mathbf{R}_{-\text{off}}\mathbf{R}_{\text{h}}^T (\mathsf{T}_a - \mathsf{B}_{\mathsf{T}}, \mathsf{T}_b - \mathsf{B}_{\mathsf{T}}, \mathsf{T}_c - \mathsf{B}_{\mathsf{T}}) + (\mathsf{B}_{\mathsf{T}}, \mathsf{B}_{\mathsf{T}}, \mathsf{B}_{\mathsf{T}}) \tag{C.32}$$

In summary, the set of points $\mathsf{T}'_{\{a,b,c\}}$ can be simply derived from the measured points $\mathsf{T}_{\{a,b,c\}}$. Their Fick angles are equal to zero when the subject is in the primary position; the plane they define is parallel to $\mathsf{H}_2 - \mathsf{H}_3$, and the forehead vector F is parallel to H_2. The real Fick angles for other head poses are computed using these corrected points, according to (C.4), (C.5) and (C.7). For the sake of simplicity, however, the notation $(')$ specifying the use of corrected points is not used elsewhere in this appendix.

Bibliography

R. S. Allison, M. Eizenman and B. S. K. Cheung. Combined head and eye tracking system for dynamic testing of the vestibular system. *IEEE Transactions on Biomedical Engineering*, 43(11): 1073–1082, 1996.

E. L. Amazeen, P. G. Amazeen, A. A. Post and P. J. Beek. Timing the selection of information during rhythmic catching. *J Mot Behav*, 31(3): 279–289, 1999.

N. A. Aspragathos and J. K. Dimitros. A comparative study of three methods for robot kinematics. *IEEE Transactions on Systems Man and Cybernetics Part B-Cybernetics*, 28(2): 135–145, 1998.

K. J. Astrom and R. M. Murray. *Feedback Systems: An Introduction for Scientists and Engineers*. `http://www.cds.caltech.edu/~murray/books/AM05/wiki/index.php`, 2005.

C. G. Atkeson, J. G. Hale, F. Pollick, M. Riley, S. Kotosaka, S. Schaal, T. Shibata, G. Tevatia, A. Ude, S. Vijayakumar and M. Kawato. Using humanoid robots to study human behavior. *IEEE Intelligent Systems and Their Applications*, 15(4): 46–55, 2000.

C. Bapat, S. Sankar and N. Popplewell. Repeated impacts on a sinusoidally vibrating table. *J Sound Vibration*, 108(1): 99–115, 1986.

P. J. Beek and A. Lewbel. The science of juggling. *Scientific American*, 273(5): 92–97, 1995.

P. J. Beek and M. T. Turvey. Temporal patterning in cascade juggling. *J Exp Psychol Hum Percept Perform*, 18(4): 934–947, 1992.

P. J. Beek and A. A. M. van Santvoord. Learning the cascade juggle - a dynamic-systems analysis. *J Mot Behav*, 24(1): 85–94, 1992.

N. Bernstein. *The coordination and regulation of movements*. Pergamon, London, 1967.

B. Brogliato, M. Mabrouk and A. Zavala-Rio. On the controllability of linear juggling mechanical systems. *Systems & Control Letters*, 55: 350–367, 2006.

B. Brogliato and A. Zavala-Rio. On the control of complementary-slackness juggling mechanical systems. *IEEE Transactions on Automatic Control*, 45(2): 235–246, 2000.

A. E. Bryson and Y. C. Ho. *Applied optimal control: optimization, estimation, and control*. Blaisdell, Waltham, MA, 1969.

J. J. Buchanan, J. H. Park and C. H. Shea. Target width scaling in a repetitive aiming task: switching between cyclical and discrete units of action. *Exp Brain Res*, 175(4): 710–725, 2006.

M. Buehler, D. Koditschek and P. Kindlmann. A one degree of freedom juggler in a two degree of freedom environment. In *IEEE/RSJ Conf. intelligent Systems and Robots*, pages pp. 91–97. Tokyo, Japan, 1988.

M. Buehler, D. Koditschek and P. Kindlmann. A family of robot control strategies for intermittent dynamical environments. *IEEE Control Systems Magazine*, 10(2): pp. 16–22, 1990.

M. Buehler, D. Koditschek and P. Kindlmann. Planning and control of robotic juggling and catching tasks. *International Journal of Robotics Research*, 13(2): 101–118, 1994.

A. Buschges. Sensory control and organization of neural networks mediating coordination of multisegmental organs for locomotion. *J Neurophysiol*, 93(3): 1127–1135, 2005.

D. E. Chang, R. Ronsse and R. Sepulchre. Is bounce juggling easier in a parabolic billiard than in a wedge ? In **D. H. van Campen, M. D. Lazurko and W. P. J. M. van den Oever**, editors, *5th Euromech Nonlinear Dynamics Conference*, pages 321–328. Eindhoven, The Nederlands, 2005.

A. H. Clarke, J. Ditterich, K. Druen, U. Schonfeld and C. Steineke. Using high frame rate cmos sensors for three-dimensional eye tracking. *Behav Res Methods Instrum Comput*, 34(4): 549–560, 2002.

A. H. Clarke, J. Ditterich, K. Druen, U. Schonfeld and C. Steineke. The chronos eye tracker: Description and verification study, 2003.

A. H. Clarke, W. Teiwes and H. Schrerer. Videooculography - an alternative method for measurement of three-dimensional eye movements. In **R. Schmid and D. Zambarbieri**, editors, *Oculomotor control and cognitive processes*, pages 431–443. Elsevier, Amsterdam, 1991.

A. Cohen, S. Rossignol and S. Grillner. *Neural Control of Rhythmic Movements in Vertebrates*. Wiley, New York, 1988.

H. Collewijn, J. Van der Steen, L. Ferman and T. C. Jansen. Human ocular counterroll: assessment of static and dynamic properties from electromagnetic scleral coil recordings. *Exp Brain Res*, 59(1): 185–196, 1985.

J. J. Collins and S. A. Richmond. Hard-wired central pattern generators for quadrupedal locomotion. *Biol Cybern*, 71(5): 375–385, 1994.

S. Collins, A. Ruina, R. Tedrake and M. Wisse. Efficient bipedal robots based on passive-dynamic walkers. *Science*, 307(5712): 1082–1085, 2005.

S. H. Collins, M. Wisse and A. Ruina. A three-dimensional passive-dynamic walking robot with two legs and knees. *International Journal of Robotics Research*, 20(7): 607–615, 2001.

J. D. Crawford, M. Z. Ceylan, E. M. Klier and D. Guitton. Three-dimensional eye-head coordination during gaze saccades in the primate. *J Neurophysiol*, 81(4): 1760–1782, 1999.

J. D. Crawford, J. Martinez-Trujillo and E. M. Klier. Neural control of three-dimensional eye and head movements. *Curr Opin Neurobiol*, 13(6): 655–662, 2003.

J. D. Crawford and T. Vilis. Axes of eye rotation and listing's law during rotations of the head. *J Neurophysiol*, 65(3): 407–423, 1991.

A. de Rugy and D. Sternad. Interaction between discrete and rhythmic movements: reaction time and phase of discrete movement initiation during oscillatory movements. *Brain Res*, 994(2): 160–174, 2003.

A. de Rugy, K. Wei, H. Muller and D. Sternad. Actively tracking 'passive' stability in a ball bouncing task. *Brain Res*, 982(1): 64–78, 2003.

J. Denavit and R. S. Hartenberg. A kinematic notation for the lower-pair mechanism based on matrices. *ASME Journal of Applied Mechanics*, pages 215–221, 1955.

M. Desmurget and S. Grafton. Forward modeling allows feedback control for fast reaching movements. *Trends Cogn Sci*, 4(11): 423–431, 2000.

M. Desmurget, H. Grea, J. S. Grethe, C. Prablanc, G. E. Alexander and S. T. Grafton. Functional anatomy of nonvisual feedback loops during reaching: a positron emission tomography study. *J Neurosci*, 21(8): 2919–2928, 2001.

V. Dietz. Do human bipeds use quadrupedal coordination? *Trends Neurosci*, 25(9): 462–467, 2002.

T. M. H. Dijkstra, H. Katsumata, A. de Rugy and D. Sternad. The dialogue between data and model: Passive stability and relaxation behavior in a ball bouncing task. *Nonlinear Studies*, 11(3): 319–344, 2004.

J. Duysens and H. W. Van de Crommert. Neural control of locomotion; the central pattern generator from cats to humans. *Gait Posture*, 7(2): 131–141, 1998.

A. Fick. Die bewegungen des menschlichen augapfels. *Zeitschrift für rationelle Medizin*, 4: 109–128, 1874.

T. Flash and N. Hogan. The coordination of arm movements: an experimentally confirmed mathematical model. *J Neurosci*, 5(7): 1688–1703, 1985.

G. Franklin, J. D. Powell and A. Emami-Naeini. *Feedback Control of Dynamic Systems*. Prentice Hall, 5th edition, 2005.

M. Gerard. *Stabilisation de tâches rythmiques: étude d'un jongleur plan*. Ph.D. thesis, Université de Liège, 2005.

M. Gerard and R. Sepulchre. Stabilization through weak and occasional interactions: a billiard benchmark. In **F. Allgower**, editor, *6th IFAC-Symposium on Nonlinear Control Systems (NOLCOS)*, pages 75–80. IFAC, Stuttgart, Germany, 2004.

M. Gerard and R. Sepulchre. Rhythmic stabilization of periodic orbits in a wedge. In **P. Horacek, M. Simandl and P. Zitek**, editors, *IFAC World Congress*. Prague, Czech Republic, 2005.

R. Goldman. Intersection of two lines in three-space. In **A. S. Glassner**, editor, *Graphics Gems*, volume I, page 304. Academic Press, San Diego, 1990.

A. Goswami, B. Thuilot and B. Espiau. A study of the passive gait of a compass-like biped robot: Symmetry and chaos. *International Journal of Robotics Research*, 17(12): 1282–1301, 1998.

J. Guckenheimer and P. J. Holmes. *Nonlinear oscillations, dynamical systems and bifurcations of vector fields*. Springer-Verlag, New York, 1986.

H. Haken, J. A. Kelso and H. Bunz. A theoretical model of phase transitions in human hand movements. *Biol Cybern*, 51(5): 347–356, 1985.

Y. H. Han, A. N. Kumar, M. F. Reschke, J. T. Somers, L. F. Dell'Osso and R. J. Leigh. Vestibular and non-vestibular contributions to eye movements that compensate for head rotations during viewing of near targets. *Exp Brain Res*, 165(3): 294–304, 2005.

C. M. Harris and D. M. Wolpert. Signal-dependent noise determines motor planning. *Nature*, 394(6695): 780–784, 1998.

L. Harris, K. Beykirch and M. Fetter. The visual consequences of deviations in the orientation of the axis of rotation of the human vestibulo-ocular reflex. *Vision Res*, 41(25-26): 3271–3281, 2001.

M. Haruno, D. M. Wolpert and M. Kawato. Mosaic model for sensorimotor learning and control. *Neural Comput*, 13(10): 2201–2220, 2001.

T. Haslwanter. Mathematics of three-dimensional eye rotations. *Vision Res*, 35(12): 1727–1739, 1995.

T. Haslwanter. *Computational and Experimental Aspects of Rotatory Eye Movements in Three Dimensions*. Habilitationsschrift, Universität Zürich, 2000.

T. Haslwanter and S. T. Moore. A theoretical analysis of three-dimensional eye position measurement using polar cross-correlation. *IEEE Trans Biomed Eng*, 42(11): 1053–1061, 1995.

M. Hatamian and D. J. Anderson. Design considerations for a real-time ocular counterroll instrument. *IEEE Trans Biomed Eng*, 30(5): 278–288, 1983.

H. Hirai and F. Miyazaki. Dynamic coordination between robots: Self-organized timing selection in a juggling-like ball-passing task. *IEEE Transactions on Systems Man and Cybernetics Part B-Cybernetics*, 36(4): 738–754, 2006.

A. L. Hodgkin and A. F. Huxley. A quantitative description of membrane current and its application to conduction and excitation in nerve. *J Physiol*, 117(4): 500–544, 1952.

P. Holmes, R. J. Full, D. Koditschek and J. Guckenheimer. The dynamics of legged locomotion: Models, analyses, and challenges. *Siam Review*, 48(2): 207–304, 2006.

P. J. Holmes. The dynamics of repeated impacts with a sinusoidally vibrating table. *J Sound Vibration*, 84(2): 173–189, 1982.

R. Huys. *Disentangling Perceptual-Motor Learning: assembly and embedding in juggling and rowing*. Ph.D. thesis, Vrije Universiteit Amsterdam, 2004.

R. Huys and P. J. Beek. The coupling between point-of-gaze and ball movements in three-ball cascade juggling: the effects of expertise, pattern and tempo. *J Sports Sci*, 20(3): 171–186, 2002.

R. Huys, A. Daffertshofer and P. J. Beek. Learning to juggle: on the assembly of functional subsystems into a task-specific dynamical organization. *Biol Cybern*, 88(4): 302–318, 2003.

V. K. Jirsa and J. A. Kelso. The excitator as a minimal model for the coordination dynamics of discrete and rhythmic movement generation. *J Mot Behav*, 37(1): 35–51, 2005.

M. I. Jordan and D. M. Wolpert. Computational motor control. In **M. Gazzaniga**, editor, *The Cognitive Neurosciences*. MIT Press, Cambridge, MA, 1999.

J. F. Kalaska, S. H. Scott, P. Cisek and L. E. Sergio. Cortical control of reaching movements. *Curr Opin Neurobiol*, 7(6): 849–859, 1997.

H. Katsumata, V. Zatsiorsky and D. Sternad. Control of ball-racket interactions in rhythmic propulsion of elastic and non-elastic balls. *Exp Brain Res*, 149(1): 17–29, 2003.

M. Kawato. Internal models for motor control and trajectory planning. *Curr Opin Neurobiol*, 9(6): 718–727, 1999.

J. A. Kelso. Phase transitions and critical behavior in human bimanual coordination. *Am J Physiol*, 246(6 Pt 2): R1000–4, 1984.

J. A. Kelso, D. L. Southard and D. Goodman. On the nature of human interlimb coordination. *Science*, 203(4384): 1029–1031, 1979.

J. A. S. Kelso. *Dynamic patterns. The self-organization of brain and behavior*. MIT Press, Cambridge, MA, 1995.

A. D. Kuo. Energetics of actively powered locomotion using the simplest walking model. *J Biomech Eng*, 124(1): 113–120, 2002a.

A. D. Kuo. The relative roles of feedforward and feedback in the control of rhythmic movements. *Motor Control*, 6(2): 129–145, 2002b.

M. F. Land and P. McLeod. From eye movements to actions: how batsmen hit the ball. *Nat Neurosci*, 3(12): 1340–1345, 2000.

H. E. Lehtihet and B. N. Miller. Numerical study of a billiard in a gravitational field. *Phys. D*, 21(1): 93–104, 1986.

A. Lewbel. Research in juggling history, 2002.

S. G. Lisberger, C. Evinger, G. W. Johanson and A. F. Fuchs. Relationship between eye acceleration and retinal image velocity during foveal smooth pursuit in man and monkey. *J Neurophysiol*, 46(2): 229–249, 1981.

K. M. Lynch and C. K. Black. Recurrence, controllability, and stabilization of juggling. *IEEE Transactions on Robotics and Automation*, 17(2): 113–124, 2001.

E. Marder. Motor pattern generation. *Curr Opin Neurobiol*, 10(6): 691–698, 2000.

E. Marder and D. Bucher. Central pattern generators and the control of rhythmic movements. *Curr Biol*, 11(23): R986–996, 2001.

K. Matsuoka. Sustained oscillations generated by mutually inhibiting neurons with adaptation. *Biol Cybern*, 52(6): 367–376, 1985.

K. Matsuoka. Mechanisms of frequency and pattern control in the neural rhythm generators. *Biol Cybern*, 56(5-6): 345–353, 1987.

E. A. Maxwell. *General Homogeneous Coordinates in Space of Three Dimensions*. Cambridge Univ. Press, Cambridge, U.K., 1951.

T. McGeer. Passive dynamic walking. *International Journal of Robotics Research*, 9(2): 62–82, 1990.

B. Mehta and S. Schaal. Forward models in visuomotor control. *J Neurophysiol*, 88(2): 942–953, 2002.

L. Menini and A. Tornambe. Control of (otherwise) uncontrollable linear mechanical systems through non-smooth impacts. *Systems & Control Letters*, 49(4): 311–322, 2003.

R. C. Miall, D. J. Weir, D. M. Wolpert and J. F. Stein. Is the cerebellum a smith predictor? *J Mot Behav*, 25(3): 203–216, 1993.

S. T. Moore, I. S. Curthoys and S. G. McCoy. Vtm–an image-processing system for measuring ocular torsion. *Comput Methods Programs Biomed*, 35(3): 219–230, 1991.

S. T. Moore, T. Haslwanter, I. S. Curthoys and S. T. Smith. A geometric basis for measurement of three-dimensional eye position using image processing. *Vision Res*, 36(3): 445–459, 1996.

K. Nakayama. Photographic determination of the rotational state of the eye using matrices. *Am J Optom Physiol Opt*, 51(10): 736–742, 1974.

R. Newman, Y. Matsumoto, S. Rougeaux and A. Zelinsky. Real-time stereo tracking for head pose and gaze estimation. In **J. L. Crowley**, editor, *4th IEEE Internat. Conf. on Automatic Face and Gesture Recognition*. IEEE, Grenoble, France, 2000.

J. J. Orban de Xivry, S. J. Bennett, P. Lefevre and G. R. Barnes. Evidence for synergy between saccades and smooth pursuit during transient target disappearance. *J Neurophysiol*, 95(1): 418–427, 2006.

D. Ott, F. Gehle and R. Eckmiller. Video-oculographic measurement of 3-dimensional eye rotations. *J Neurosci Methods*, 35(3): 229–234, 1990.

J. A. Parker, R. V. Kenyon and L. R. Young. Measurement of torsion from multitemporal images of the eye using digital signal processing techniques. *IEEE Trans Biomed Eng*, 32(1): 28–36, 1985.

F. Plestan, J. W. Grizzle, E. R. Westervelt and G. Abba. Stable walking of a 7-dof biped robot. *IEEE Transactions on Robotics and Automation*, 19(4): 653–668, 2003.

A. A. Post, A. Daffertshofer and P. J. Beek. Principal components in three-ball cascade juggling. *Biol Cybern*, 82(2): 143–152, 2000.

M. H. Raibert. *Legged robots that balance.* The MIT Press series in artificial intelligence. MIT Press, Cambridge, Mass., 1986.

A. A. Rizzi and D. E. Koditschek. Progress in spatial robot juggling. In *IEEE International Confererence on Robotics and Automation*, pages 775–780. Nice, France, 1992.

A. A. Rizzi and D. E. Koditschek. Further progress in robot juggling : The spatial two-juggle. In *IEEE International Confererence on Robotics and Automation*, volume 3, pages 919–924. Atlanta, GA, 1993.

A. A. Rizzi, L. L. Whitcomb and D. E. Koditschek. Distributed real-time control of a spatial robot juggler. *Computer*, 25(5): 12–24, 1992.

D. A. Robinson. A method of mesuring eye movement using a scleral search coil in a magnetic field. *IEEE, Trans Biomed Eng*, BME-10: 137–145, 1963.

R. Ronsse, P. Lefevre and R. Sepulchre. Open-loop stabilization of 2d impact juggling. In **F. Allgower**, editor, *6th IFAC-Symposium on Nonlinear Control Systems (NOLCOS)*, pages 1157–1162. IFAC, Stuttgart, Germany, 2004.

R. Ronsse, P. Lefevre and R. Sepulchre. Timing feedback control of a rhythmic system. In **E. F. Camacho, P. J. Fleming and S. Yurkovich**, editors, *44th IEEE Conference on Decision and Control and European Control Conference ECC 2005*, pages 6146–6151. IEEE, Seville, Spain, 2005.

R. Ronsse, P. Lefevre and R. Sepulchre. Sensorless stabilization of bounce juggling. *IEEE Transactions on Robotics*, 22(1): 147–159, 2006.

R. Ronsse, P. Lefevre and R. Sepulchre. Rhythmic feedback control of a blind planar juggler. *IEEE Transactions on Robotics*, in press, 2007a.

R. Ronsse, P. Lefevre and R. Sepulchre. Robotics and neuroscience: a rhythmic interaction. *Neural Netw*, submitted, 2007b.

R. Ronsse and R. Sepulchre. Feedback control of impact dynamics: the bouncing ball revisited. In **P. Mistra and R. Middleton**, editors, *45th IEEE Conference on Decision and Control*, pages 4807–4812. San Diego, CA, 2006.

R. Ronsse, J.-L. Thonnard, P. Lefevre and R. Sepulchre. Trading performance for robustness in rhythmic movements. submitted, 2007c.

R. Ronsse, O. White and P. Lefevre. Computation of gaze orientation under unrestrained head movements. *J Neurosci Methods*, 159(1): 158–169, 2007d.

P. Sabes. The planning and control of reaching movements. *Curr Opin Neurobiol*, 10: 740–746, 2000.

U. Saranli, M. Buehler and D. Koditschek. Rhex - a simple and highly mobile hexapod robot. *International Journal of Robotics Research*, 20(7): 616–631, 2001.

S. Schaal and C. G. Atkeson. Open loop stable control strategies for robot juggling. In *IEEE International Conference on Robotics and Automation*, volume 3, pages 913–918, 1993.

S. Schaal, C. G. Atkeson and D. Sternad. One-handed juggling: A dynamical approach to a rhythmic movement task. *J Mot Behav*, 28(2): 165–183, 1996.

S. Schaal and N. Schweighofer. Computational motor control in humans and robots. *Curr Opin Neurobiol*, 15(6): 675–682, 2005.

S. Schaal, D. Sternad, R. Osu and M. Kawato. Rhythmic arm movement is not discrete. *Nat Neurosci*, 7(10): 1136–1143, 2004.

G. Schoner. A dynamic theory of coordination of discrete movement. *Biol Cybern*, 63(4): 257–270, 1990.

G. Schoner and J. A. Kelso. Dynamic pattern generation in behavioral and neural systems. *Science*, 239(4847): 1513–1520, 1988.

K. Schreiber and T. Haslwanter. Improving calibration of 3-d video oculography systems. *IEEE Trans Biomed Eng*, 51(4): 676–679, 2004.

S. H. Scott. Optimal feedback control and the neural basis of volitional motor control. *Nat Rev Neurosci*, 5(7): 532–546, 2004.

S. H. Scott and K. E. Norman. Computational approaches to motor control and their potential role for interpreting motor dysfunction. *Curr Opin Neurol*, 16(6): 693–698, 2003.

R. Sepulchre and M. Gerard. Stabilization of periodic orbits in a wedge billiard. In **D. A. Lawrence and T. Parisini**, editors, *42nd IEEE Conference on Decision and Control*, pages 1568–1573. IEEE, Hawaii, 2003.

C. E. Shannon. Scientific aspects of juggling. In **N. J. A. Sloane and A. D. Wyner**, editors, *Claude Elwood Shannon : collected papers*, page 924. IEEE Press, New York, 1993.

S. W. Shih and J. Liu. A novel approach to 3-d gaze tracking using stereo cameras. *IEEE Trans Syst Man Cybern B Cybern*, 34(1): 234–245, 2004.

M. W. Spong. Bipedal locomotion, robot gymnastics, and robot air hockey: A rapprochement. In *Super-Mechano Systems (SMS'99) Workshop*. Tokyo, Japan, 1999.

M. W. Spong. Impact controllability of an air hockey puck. *Systems and Control Letters*, 42(5): 333–345, 2001.

D. Sternad. Juggling and bouncing balls: Parallels and differences in dynamic concepts and tools. *International Journal of Sport Psychology*, 30(4): 462–489, 1999.

D. Sternad, W. J. Dean and S. Schaal. Interaction of rhythmic and discrete pattern generators in single-joint movements. *Hum Mov Sci*, 19(4): 627–664, 2000.

D. Sternad, M. Duarte, H. Katsumata and S. Schaal. Bouncing a ball: tuning into dynamic stability. *J Exp Psychol Hum Percept Perform*, 27(5): 1163–1184, 2001a.

D. Sternad, M. Duarte, H. Katsumata and S. Schaal. Dynamics of a bouncing ball in human performance. *Physical Review E*, 6301(1): art. no.–011902, 2001b.

S. H. Strogatz. *Sync: The Emerging Science of Spontaneous Order*. Hyperion, New York, 2003.

S. P. Swinnen. Intermanual coordination: from behavioural principles to neural-network interactions. *Nat Rev Neurosci*, 3(5): 348–359, 2002.

S. P. Swinnen and N. Wenderoth. Two hands, one brain: cognitive neuroscience of bimanual skill. *Trends Cogn Sci*, 8(1): 18–25, 2004.

M. Tlili, D. Mottet, M. A. Dupuy and B. Pavis. Stability and phase locking in human soccer juggling. *Neurosci Lett*, 360(1-2): 45–48, 2004.

E. Todorov. Optimality principles in sensorimotor control. *Nat Neurosci*, 7(9): 907–915, 2004.

E. Todorov. Optimal control theory. In **K. Doya, S. Ishii, A. Pouget and R. P. Rao**, editors, *Bayesian Brain*. MIT Press, Cambridge, MA, 2006.

E. Todorov and M. I. Jordan. Optimal feedback control as a theory of motor coordination. *Nat Neurosci*, 5(11): 1226–1235, 2002.

A. Tornambe. Modeling and control of impact in mechanical systems: Theory and experimental results. *IEEE Transactions on Automatic Control*, 44(2): 294–309, 1999.

N. Tufillaro, T. Abbott and J. Reilly. *An experimental approach to nonlinear dynamics and chaos*. Addison-Wesley studies in nonlinearity. Addison-Wesley, Redwood City, CA, 1992.

N. B. Tufillaro and A. M. Albano. Chaotics dynamics of a bouncing ball. *Am J Phys*, 54(10): 939–944, 1985.

M. T. Turvey. Coordination. *Am Psychol*, 45(8): 938–953, 1990.

D. Tweed, W. Cadera and T. Vilis. Computing three-dimensional eye position quaternions and eye velocity from search coil signals. *Vision Res*, 30(1): 97–110, 1990.

D. Tweed and T. Vilis. Implications of rotational kinematics for the oculomotor system in three dimensions. *J Neurophysiol*, 58(4): 832–849, 1987.

A. M. van Mourik and P. J. Beek. Discrete and cyclical movements: unified dynamics or separate control? *Acta Psychol (Amst)*, 117(2): 121–138, 2004.

J. Van Opstal. Representation of eye position in three dimensions. In **A. Berthoz**, editor, *Multisensory control of movement*, pages 27–41. Oxford University Press, Oxford, 1993.

A. A. M. van Santvoord and P. J. Beek. Spatiotemporal variability in cascade juggling. *Acta Psychologica*, 91(2): 131–151, 1996.

T. Vieville and D. Masse. Ocular counter-rolling during active head tilting in humans. *Acta Otolaryngol*, 103(3-4): 280–290, 1987.

T. L. Vincent and A. I. Mees. Controlling a bouncing ball. *International Journal of Bifurcation and Chaos*, 10(3): 579–592, 2000.

J. G. Wang and E. Sung. Study on eye gaze estimation. *IEEE Transactions on Systems Man and Cybernetics Part B-Cybernetics*, 32(3): 332–350, 2002.

K. Wei, T. M. H. Dijkstra and D. Sternad. Passive stability, perturbations, and active control in a rhythmic task. In *Society for Neuroscience 36th Annual Meeting*. Atlanta, GA, 2006.

E. R. Westervelt, G. Buche and J. W. Grizzle. Experimental validation of a framework for the design of controllers that induce stable walking in planar bipeds. *International Journal of Robotics Research*, 23(6): 559–582, 2004.

O. White, Y. Bleyenheuft, R. Ronsse, A. M. Wing, P. Lefevre and J.-L. Thonnard. Altered gravity highlights central pattern generators mechanisms. submitted, 2007.

D. Wolpert, R. Miall and M. Kawato. Internal models in the cerebellum. *Trends Cogn. Sci.*, 2(9): 338–347, 1998.

D. M. Wolpert and Z. Ghahramani. Computational principles of movement neuroscience. *Nat Neurosci*, 3 Suppl: 1212–1217, 2000.

D. M. Wolpert and M. Kawato. Multiple paired forward and inverse models for motor control. *Neural Netw*, 11(7-8): 1317–1329, 1998.

D. M. Wolpert and R. C. Miall. Forward models for physiological motor control. *Neural Netw*, 9(8): 1265–1279, 1996.

D. H. Yoo and M. J. Chung. A novel non-intrusive eye gaze estimation using cross-ratio under large head motion. *Computer Vision and Image Understanding*, 98(1): 25–51, 2005.

L. H. Yu and M. Eizenman. A new methodology for determining point-of-gaze in head-mounted eye tracking systems. *IEEE Transactions on Biomedical Engineering*, 51(10): 1765–1773, 2004.

D. Yuksel, L. M. Optican and P. Lefevre. Properties of saccades in duane retraction syndrome. *Invest Ophthalmol Vis Sci*, 46(9): 3144–3151, 2005.

A. Zavala-Rio and B. Brogliato. On the control of a one degree-of-freedom juggling robot. *Dynamics and Control*, 9(1): 67–90, 1999.

A. Zavala-Rio and B. Brogliato. Direct adaptive control design for one-degree-of-freedom complementary-slackness jugglers. *Automatica*, 37(7): 1117–1123, 2001.

E. P. Zehr, T. J. Carroll, R. Chua, D. F. Collins, A. Frigon, C. Haridas, S. R. Hundza and A. K. Thompson. Possible contributions of cpg activity to the control of rhythmic human arm movement. *Can J Physiol Pharmacol*, 82(8-9): 556–568, 2004.

D. Zhu, S. T. Moore and T. Raphan. Robust pupil center detection using a curvature algorithm. *Comput Methods Programs Biomed*, 59(3): 145–157, 1999.